ANALYSIS AND COMPUTATIONAL MODELLING OF DROP FORMATION FOR PIEZO-ACTUATED DOD MICRO-DISPENSER

SHI MIN

MASTER OF ENGINEERING

DEPARTMENT OF MECHNICAL ENGINEERING
NATIONAL UNIVERSITY OF SINGAPORE

2008

Acknowledgements

First, I would like to express my sincere appreciation to my supervisors A/ Prof Wong Yoke San and A/Prof Jerry Fuh for their vigorous suggestions and discussions during the research, and for their kind help and supports when I faced difficulties. I appreciate that they gave me this opportunity to widen my view on how to do the research, and to learn a lot through these two years. I am also grateful to A/Prof Loh Han Tong for his kind guidance.

I would also like to thank A/Prof Sigurdur Tryggvi Thoroddsen, for his time and patience in answering my questions, and for his considerable help on the experiments of this study.

Many thanks to the members of DOD group at CIPMAS Lab: Jinxin, Stanley, Yuan Song, Ya Qun, Xu Qian and Amir, for their helpful group discussions and comments.

Give my sincere thanks to Mr. Wang Junhong, who works at Computer Center of NUS. He gave me an enormous assistance in learning and problem solving about the software.

Deepest gratitude is given to my parents and grandmother for their support and love forever.

Table of Contents

Summary

The 3D Inkjet printing is a rapid prototyping technology that is becoming an increasingly attractive technology for a diversity of applications in recent years, due to its advantages in high resolution, low cost, non-contact, ease of material handling, compact in machine size, and environmental benignity. There are two primary methods of inkjet printing: continuous inkjet (CIJ), and drop-on-demand inkjet (DOD). The DOD inkjet method is given particular attention because DOD systems have no fluid recirculation requirement, and this makes their use as a general fluid microdispensing technology more straightforward than continuous mode technology.

The print quality is closely related to the characteristic of the droplet ejected from the printhead. In order to improve the accuracy of the simulation model, an analytical method is used to analyze the oscillatory fluid movement inside a squeezed-type piezoelectric cylindrical inkjet print head with tapered nozzle. Unlike the earlier researcher, instead of a single unit, the printhead is treated as four parts: unactuated part1 (without connecting with the nozzle part), actuated part1, unactuated part 2 (connected with the actuated part and the nozzle part) and nozzle part. The pressure and velocity functions for each part are derived and these functions with unknown coefficients are solved together with the experimentally obtained upstream pressure boundary condition of a back pressure, neither applying zero pressure nor regarding the capillary glass tube as semi-infinite tube. The axial velocity history at the nozzle

exit is obtained in the form of an oscillatory function in time domain. It is recommended that 40 Fourier terms be used for the computation and simulation, since it shows the advantage of compromise of time-saving and good simulation results.

In this thesis, a two-dimensional axisymmetric numerical simulation model of the drop formation from the nozzle has been developed with the Volume-of-Fluid (VOF) method and the Piecewise-Linear Interface Calculation (PLIC) technique. Continuous Surface Force (CFS) method is used to take into consideration of the surface tension effect. The advanced computational fluid dynamic software packages, FLUENT and Gambit, are used to carry out the simulation and modeling of the drop formation. Gambit generates the geometry and mesh, while FLUENT simulates and models the process of the drop formation. The driving signal applied to the piezo-actuated capillary is simulated via a Fluent-C program by using the User Defined Function (UDF) of FLUENT.

The experimental system used in this research is made up of an XYZ-motion stage with a single print-head, temperature control, pneumatic control, a high-speed camera, and a computer with a user interface to coordinate its motion and dispensing.

The thesis presents a detailed description of the three main stages during the drop ejection process, and discusses the effect of the Reynolds number and Capillary number on the dynamics of drop formation. To evaluate the precision of this model,

simulation and experimental results of de-ionized water and PEDOT are compared as the fluid materials. The comparison shows that the percentage error of drop volume and velocity are within the error range of ±20%.

List of Tables

List of Figures

List of Symbols

$C_1, C_2, C_3, C_4, C_5, C_6, C_7, C_8$	unknown coefficients
E_C	Young's modulus of a capillary glass tube
$J_n()$	Bessel functions of the first kind
$P(z)$	pressure function
V	applied voltage
$V_z(r,z)$	axial velocity
c_f	intrinsic speed of sound in a liquid
$c_{11}^E, c_{13}^E, c_{33}^E$	elastic stiffness of a PZT actuator at constant electric field
e_{31}^E, e_{33}^E	piezoelectric constant at constant electric field
i	imaginary number
r_0	orifice radius
r_1	inner radius of a capillary glass tube
r_2	outer radius of a capillary glass tube
r_3	inner radius of a PZT actuator
$r_4(z) = r_1 - z\tan(\theta)$	varying radius at the nozzle
$u^C(r,z)$	radial displacement of a capillary glass tube
ν_C	Poisson's ratio of a capillary glass tube
ν_f	kinematic viscosity
θ	tapering angle
μ_f	dynamics viscosity

ρ_f	liquid density
σ_f	surface tension
$\sigma_r^C(r,z)$	radial stress of a capillary glass tube
ω	angular frequency

Chapter 1 Introduction

1.1 Rapid Prototyping

Rapid Prototyping (RP) Technology developed since 1980s is a generic group of emerging technologies that enable “rapid” fabrication of engineering components targeted for prototyping applications. RP technology is quite different from the conventional manufacturing method of material removing. Based on the concept of material addition, RP is an advanced manufacturing technology that integrates computer-aided design (CAD), mechatronics, numerical control, material knowledge, and laser or other technologies.

RP process starts with the slicing of the model in computer. With computer control, the materials are selectively cured, cut, sintered or ejected through laser or other technologies, such as melting, heating or inkjet printing, to form the cross sections of the model, and the 3D model is also built layer by layer. Five of the popular and well-known RP techniques that are available in the market include stereo- lithography (SLA), selective laser sintering (SLS), fused deposition modeling (FDM), laminated object manufacturing (LOM), and 3D inkjet printing.

An advantage of rapid prototyping in fact is that the same data used for the prototype creation can be used to go directly from prototype to production, minimising further source of human errors. Other reasons of Rapid Prototyping are to increase effective

communication, decrease development time, decrease costly mistakes, and minimize sustaining engineering changes and to extend product lifetime by adding necessary features and eliminating redundant features early in the design.

1.2 3D Inkjet Printing

3D Inkjet printing is becoming an increasingly attractive technology for a diversity of applications in recent years, due to its advantages in high resolution, low cost, non-contact, ease of material handling, compact in machine size, and environmental benignity. There are two primary methods of inkjet printing: continuous inkjet (CIJ), and drop-on-demand inkjet (DOD). The so-called “drop-on-demand’’ inkjet method also uses small droplets of ink but the drops are ejected only when needed for printing based on pulses applied to a piezo-actuator.

3D Inkjet Printing has a great potential in commercial applications, for instance[1-3]:

- ✧ Making Flexible electronics like flexible PCBs and Organic Field Effect Transistors (OFET) by dispensing polymer comprising nanometer semiconductive particles in designed pattern without photolithography;
- ✧ Fabricating flat panel display screen by using microdispenser to directly deposit patterned organic light-emitting diodes (OLED) (Figure 1.1). Such screen promise to be brighter, thinner, lower-powered, more flexible and less expensive;
- ✧ Dispensing solder paste droplets in designed pattern for surface mount and bonding by elimination of photomask;

- ✧ Laying down microarrays of samples droplets for DNA research and drug discovery;
- ✧ Low cost consumable electronics like RFID tags.

Figure 1.1: 40" OLED TV unveiled by Seiko-Epson.

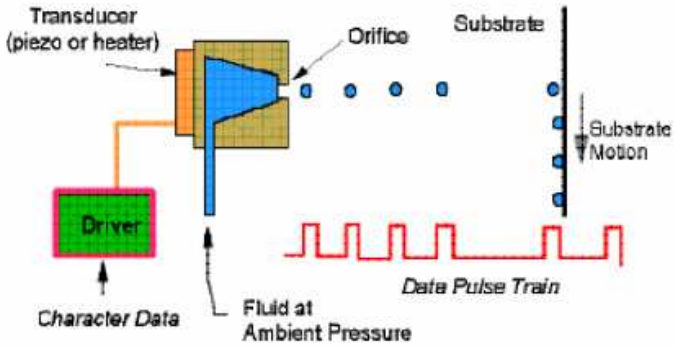

Figure 1.2: Schematic of a DOD system (www.microfab.com)

As shown in Figure 1.2, when a voltage pulse is applied across the transducer, an acoustic wave would be generated inside the chamber. This wave ejects ink droplets from a reservoir through a nozzle. The acoustic wave can be generated thermally or piezoelectrically. Thermal transducer is heated locally to form a rapidly expanding

vapor bubble that ejects an ink droplet. Piezoelectric-driven DOD bases on the deformation of some piezoelectric material to produce a sudden volume change and hence generate an acoustic wave.

The print quality is closely related to the characteristic of the droplet ejected from the inkjet printhead. In order to gain the optimal droplet size and velocity, it is desirable to understand the drop formation process. It is generally recognized that the pressure response and velocity variation inside the fluid flow channel are the key features in the development of simulation of drop formation.

1.3 Research Objectives

The main objectives of this project are:

1) To model and simulate the drop formation process from the orifice of the micro-dispenser;
2) To analysis the pressure and velocity of fluid inside the chamber and determine the downstream pressure and axial velocity boundary condition at the nozzle tip;
3) To identify the number of Fourier series terms for decomposing the voltage pulse in time domain;
4) To investigate the influence of surface tension, inertial force and viscous force on the dynamics of drop formation in terms of the Reynolds number and Capillary number;

5) To verity the accuracy of the model by comparing the velocity and diameter drop volume of ejected droplets obtained by simulation and experimentally.

1.4 Organization of the Thesis

This report starts with an introduction to the project in Chapter 1 followed by Chapter 2 that provides a literature review on inkjet printing, various micro dispensing techniques and principles as well as the formation of the droplets. Chapter 3 analyses the fluid behavior inside the channel to obtain the pressure or axial velocity history at the nozzle, which is used as the pressure or velocity boundary condition for the modeling of the drop formation process. Chapter 4 introduces the Volume of Fluid (VOF) method and Piecewise Linear Interface Calculation (PLIC) scheme used for the generation and analysis of the drop formation and describes the model developed in FLUENT. Chapter 5 gives a general outline of the experimental system. Chapter 6 explains and discusses the numerical simulation results of the proposed model and verifies the accuracy of the model by comparing the numerical and experimental results. Chapter 7 concludes on the project and puts forward a number of recommendations for future direction of research.

Chapter 2 Literature Review

2.1 Inkjet Printing Technologies

There are two primary methods of inkjets for printing: continuous inkjet and drop-on-demand (DOD) inkjet. The DOD types can be further subdivided as piezoelectric and thermal inkjet printing.

The most important material properties of inkjet printing are the viscosity and surface tension. The viscosity should be better below 20mPa s. For a given pressure wave, the lower the viscosity, the greater the velocity is and the amount of fluid expelled outside. The surface tension influences the spheroidal shape of the drop ejected from the nozzle. The suitable range of surface tension is from 28 mN m^{-1} to 350 mN m^{-1}. [3]

2.1.1 Continuous Inkjet

The first patent on the idea of continuous inkjet method was filed by William Thomson in 1867. The first commercial model of continuous inkjet printing was introduced in 1951 by Siemens. [1] In continuous ink jet technology, the ink is ejected from a reservoir through a microscopic nozzle by a high-pressure pump, creating a continuous stream of ink droplets. Some of the ink droplets will be selectively charged by a charging electrode as they form. The charged droplets are deflected to the substrate for printing, or are allowed to continue on straight to a collection gutter

for recycling, when the droplets pass through an electrostatic field.

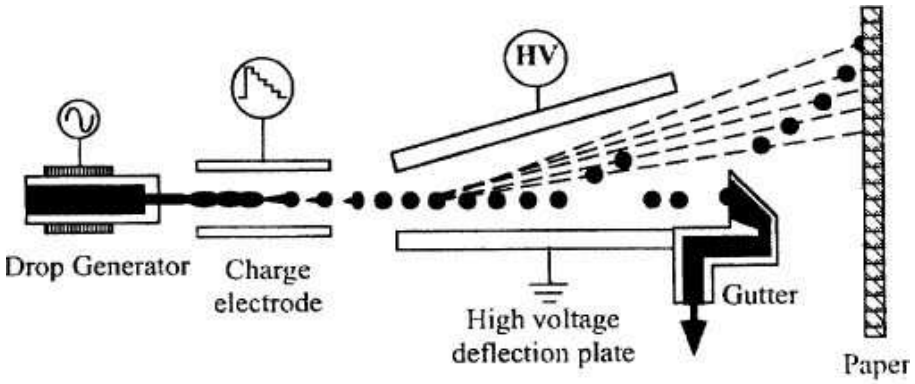

Figure 2.1: Continuous inkjet printing (www.image.com)

Continuous inkjet printing is largely used for graphical applications, e.g. textile printing and labeling due to its advantage of the very high velocity (~50 m/s) of the ink droplets. [1] [3] But, there are some drawbacks in this method, such as being expensive and difficult to maintain, and rechargeable ink required. [2]

2.1.2 Thermal Inkjet

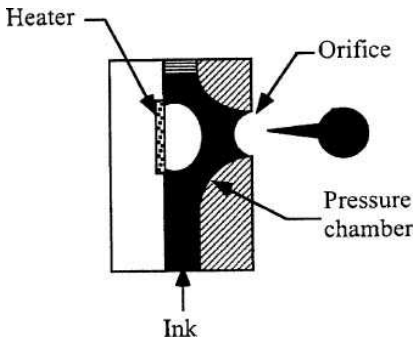

Figure 2.2: Thermal inkjet printing (www.image.com)

Thermal Inkjet technology was evolved independently by Cannon and HP. [2] In this approach, a drop is ejected from a nozzle upon an acoustic pulse generated by the

expansion of a vapor bubbles produced on the surface of the heating element. The ink used is usually water-soluble pigment or dye-based, but the print head is produced usually at less cost than other inkjet technologies.

2.1.3 Piezoelectric Inkjet

Piezoelectric inkjet printing was the first DOD technology to be developed. When a voltage is applied, the piezoelectric material deforms to generate a pressure pulse in the fluid, forcing a droplet of ink from the nozzle. Piezoelectric inkjet allows a wider variety of ink than thermal or continuous inkjet but is more expensive. The emerging inkjet material deposition market uses ink jet technologies, typically piezoelectric inkjet, to deposit materials on substrates.

According to the deformation mode, the piezoelectric inkjet printing can be classified into four types: squeeze mode, bend mode, push mode and shear mode (Fig. 2.3).[4] For squeeze mode (a), the piezoelectric ceramic tube is polarized radially, which is provided with electrodes on its inner and outer surfaces. In bend mode (b), a conductive diaphragm with deflection plate made of piezoelectric ceramics forms one side of the chamber. Applying a voltage to the piezoelectric plate results in a contraction of the plate and causing the diaphragm to flex inwardly to expel the droplet from the orifice. In push mode design (c), the piezoelectric ceramic rods expand to push against a diaphragm to eject the droplets from an orifice. In a shear mode printhead (d-f), the electric field is designed to be perpendicular to the

polarization of the piezoceramics.

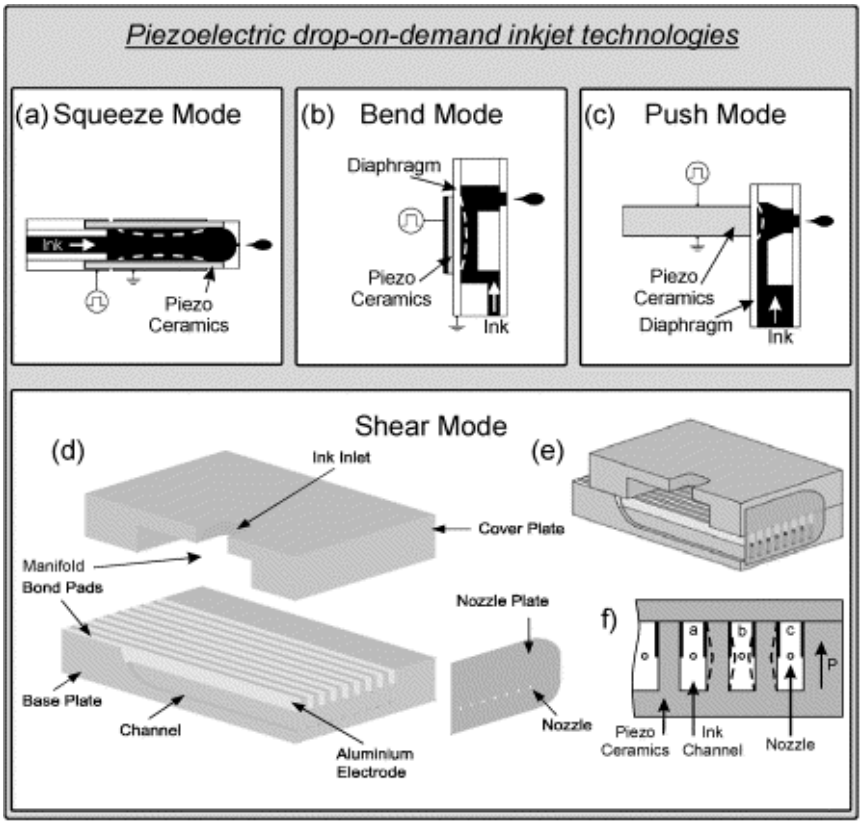

Figure 2.3: Basic map of piezoelectric DOD inkjet technologies

2.1.4 Applications

In the field of electronic manufacturing, inkjet printing technology has been used to fabricate thin-film transistors, dielectrics and circuits. Baytron-P, consisting of conducting oligomeric poly counter-ions, is a frequently used polymer. [2] Inkjet printing has evolved to make the manufacturing of multicolor polymer light-emitting diode (PLED) become feasible. [2] [3] In the field of medical diagnostic, for the creation of a DNA microarray, inkjet technology is superior to pin tools because of its smaller spot size, higher rate of throughput, and non-contact delivery. Oral dosage forms for controlled drug release are manufactured by three-dimensional inkjet printing. In

three-dimensional inkjet printing, ceramics particles with a polymeric binder solution are printed to form some ceramic shape layer-by-layer. [2] [3]

2.2 Analysis of Drop Formation

2.2.1 Experimental Analysis

In early experimental studies shown in fig 2.4, Clift et al. [5] observed that the volume of a pendant drop increases by the following addition of the drop liquid from the tube. When a drop is necking and about to break, the large part of the drop falls quickly suddenly and the drop neck breaks off from the capillary until the volume of the drop exceed a critical value of the volume and the internal axial velocity is found to attain a maximum at the breakup point. The velocity can be locally increased by several orders of magnitude due to occurrence of extremely large capillary pressure near breakup.

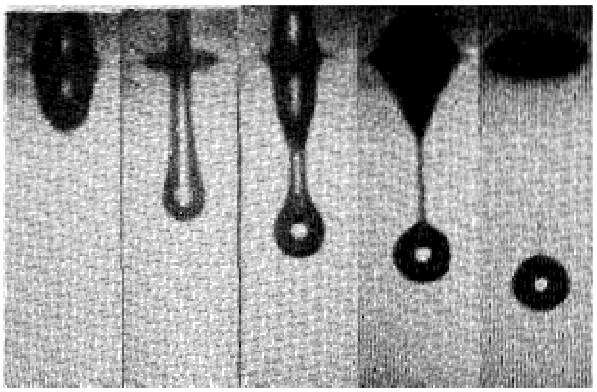

Figure 2.4: Typical process of drop formation from a tube

The experiment of the dynamics of the filament breakup was investigate by Peregrine et al. [6] Their results in Figure 2.5 show the process of double breakage of the liquid

thread with the photos during breakup of the thread. The thread breaks at its lower end by the weight of a detaching drop, where the thread joins with the falling drop to form the primary drop. Because unbalanced capillary forces exist on the thread after its first breakup, the thread recoils. The occurrence of the secondary breakup at its upper end leads to the generation of satellite droplets.

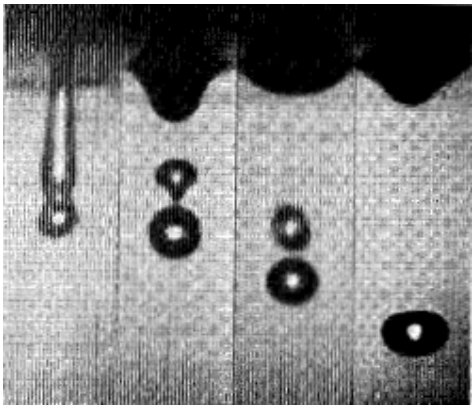

Figure 2.5: Satellite formation process

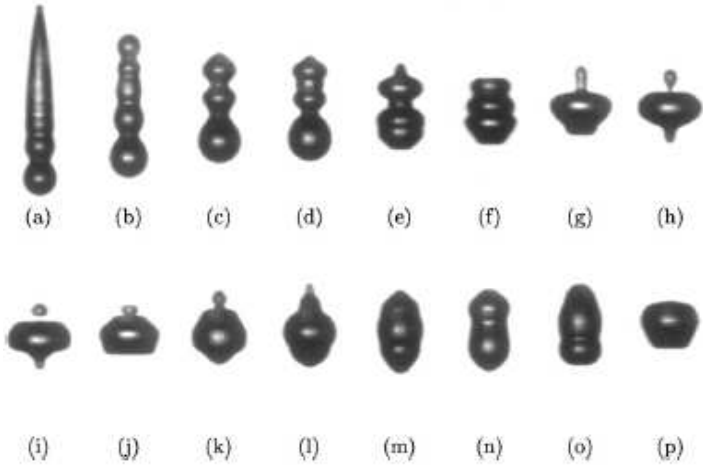

Figure 2.6: Evolution in time of satellites

As shown in Figure 2.6, Notz et al. [7] used high-speed camera to investigate the

different shapes of satellite drop in the formation as the thread breaks off. Henderson et al. [8] experimentally studied the breakup of the thread between the falling drop and the main thread and found that the secondary thread becomes unstable as evidenced by wave-like disturbances. The actual pinch-off does not occur at the point of attachment between the secondary thread and the drop. Instead, it occurs between the disturbances on the secondary thread. Kowalewski [9] also conducted experiment similar to Henderson's and investigated the related problem of the detail of the thin neck joining the droplet to its body in terms of the fluid viscosity and jet diameter. As the viscosity increased, the neck rapidly elongated and created a long thread. The thread diameter seemed to be constant within a wide range of parameters varied before rupture.

The effects of all physical parameters related to drop formation were studied experimentally by Zhang and Basaran [10], such as flow rate, inner and outer radii of the capillary and the fate of satellites. They found that the length of the liquid thread that forms during necking and breakup of a growing or forming drop is increased considerably by increasing liquid viscosity, liquid flow rate, and outer radius of the tube. Their findings are of significant fundamental and technological importance, as the length of thread grows, the thread can attain a larger volume before its breakup, thereby creating, in turn, a satellite drop having a larger volume.

Many researchers [11] [12] have carried out numerous experiments by visualization

means to examine the detail flow patterns and the variations around a forming drop with different physical and operating parameters. In these experiments, they uncovered that the flow patterns are sensitively affected by the conditions of drop formation, in particular to viscous forces. However, due to the experimental difficulties and restrictions, those studies did not completely describe the relationship between flow patterns and operating conditions. Pilch et al. [13] and Gelfand [14] conducted experiments to investigate the flow pattern. Their experimental results have demonstrated five distinct mechanisms of drop breakup as determined by initial Weber number, illustrated in Figure 2.7.

(1) Vibrational breakup We ≤ 12

(2) Bag breakup 12 < We ≤ 50

(3) Bag-and-stamen breakup 50 < We ≤ 100

(4) Sheet stripping 100 < We ≤ 350

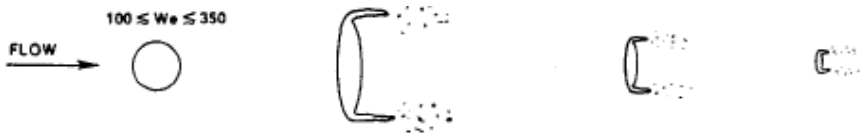

(5) Wave crest stripping followed by catastrophic breakup We > 350

Figure 2.7: Breakup mechanisms

It is well known from experiments that two dimensionless numbers, namely Weber number and Reynolds number, have dominant influence on the dynamics of drop breakup. [13] [14] The Weber number, which represents the ratio of pressure drag to interfacial tension force, is defined as $We = \rho_c d_0 U_0^2 / \sigma$, and the Reynolds number, which represents is the ratio of inertial forces to viscous forces, is defined as $\mathrm{Re} = v_s L / \nu$, where d_0 and U_0 denote the initial drop diameter and the relative initial velocity, respectively, ρ_c is the density of the ambient fluid, σ is the interfacial tension coefficient, v_s is mean fluid velocity, L is characteristic length and ν is kinematic fluid viscosity. Sometimes, Ohnesorge number is used, which represents the ratio of viscous force to interfacial tension force, as $On = \mu_d / (\rho_d d_0 \sigma)^{1/2}$, where μ_d is the viscosity of the drop fluid.

Shi et al. [15] carried out a detailed experiment of the evolution of drop formation. They revealed that the drop viscosity plays an important role in producing changes in drop shapes at breakup and lengthening of the liquid threads. The standard for measure of the liquid in inkjet printing is the shear viscosity. When the ink is a Newtonian liquid, the shear viscosity is appropriate to characterize the fluid flow. For inks that are

solutions of a high molecular weight polymer in small concentrations in a solvent, the shear viscosity cannot completely represent the behavior of these solutions. These solutions become non- Newtonian according to the definition of Newtonian fluid, which is the shear stress is proportional to the velocity gradient perpendicular to the direction of shear. Huang [16] investigated behavior of non-Newtonian solutions and found that more energy is needed to eject the droplet and some droplets are formed with a filament, which can break up into satellite droplets. This is because a small concentration of a high molecular weight polymer in a solvent can increase the elongational viscosity substantially.

The use of low viscosity elastic liquids has been focused in recent work. In Brenner et al.'s experiments, they observed the dynamics of the drop with a low viscosity fluid before and after breakup. [17] Moreover, investigators found that low-viscosity elastic liquids have a significant impact on a wide range of extension-dominated flows, especially when compared to a Newtonian fluid of the same viscosity. These fluids typically have a shear viscosity between that of water and 10 cP, and are constructed by adding a small amount of polymer to a Newtonian solvent. [18-22] In particular, the viscosity effect can be neglected at On $\leqslant$ 0.1, which is the case for almost all Newtonian fluids. [13]

2.2.2 Theoretical and Computational Analysis

In 1878, the drop formation was studied by Lord Rayleigh considering the breakup of

an invisicid cylindrical jet into drops. [23] In his work on drop formation, he used a reference system where the cylinder of liquid was initially at rest and the perturbation applied was spatially periodic. Under appropriate circumstances, surface tension forces broke the liquid into equally spaced drops. He linearized his equations with the assumption that variation of the jet radius was small compared to the radius itself. Although this assumption is invalid, Rayleigh's work has given much insight into the phenomenon of drop breakup.

Pioneering studies by a number of authors [24-26] theoretically analyzed the drop falling based primarily on macroscopic force balances. They presumed that there were two stages in the drop formation process. The first stage starts with a static growth of the drop and ends with a loss of balance of forces. The second stage takes place with the necking and breaking of the drop from the nozzle. They made a preliminary conclusion that the volume of the drops depends on the nozzle size, liquid properties and liquid flow rate through the nozzle.

2.2.2.1 1D Analysis

1D formulation of drop formation has gained popularity by numerous investigators in recent years. 1D inviscid slice model was developed by Lee [31], which is a set of equations that have been averaged across the thickness of a jet of an inviscid liquid, which has no resistance to shear stress. However, Schulkes [32] [33] found that this model is limited by the amplitude approximation which ceases to be valid while the

short-wavelength effect become increasingly important. Eggers provided a comprehensive review of the computational and experimental works on dynamics of drop formation. [37] However, a remaining question stilled unanswered, whether the surface of a drop of finite viscosity can overturn, as his description about overturning was based on the inviscid theory.

Finally, the correct set of 1D equations including viscosity was developed independently by Bechtel et al. [34], Eggers and Dupont [35], and Papageorgiou [29]. Eggers and Dupont solved one-dimensional equations based on the derivation from the Navier-Stokes system by extending the velocity and pressure variables in a Taylor series in the radial direction and retaining only the lowest-order terms in these expansions. They also made a comparison between their predictions using 1D model with other experiments of drop breaking and jetting from a nozzle. By solving the equations derived by Eggers and Dupont, Shi et al. [15] demonstrate computationally that a string of necks can be produced from the main thread. 1D equations were solved in asymptotical form to calculate the solutions of the Navier–Stokes equations before and after breakup. [36]

.

A 1D model based on simplification of the governing 2D system results in considerable saving in computation time compared to that by 2D algorithms. [38] The accuracy of this 1D model has also been verified by comparing predictions made with 1D and 2D algorithms based on the finite element method, which has shown the

agreement with experiment measured with better than 2% accuracy. [39] The difference in 1D and 2D formulations is the way in which inflow boundary conditions are imposed. A plug flow condition is imposed at the exit in the 1D model, the 2D model provides the Hagen-Poiseuille flow condition for the tube exit. Figure 2.8 clearly shows the deviation between the predictions of 1D and 2D analyses. [39]

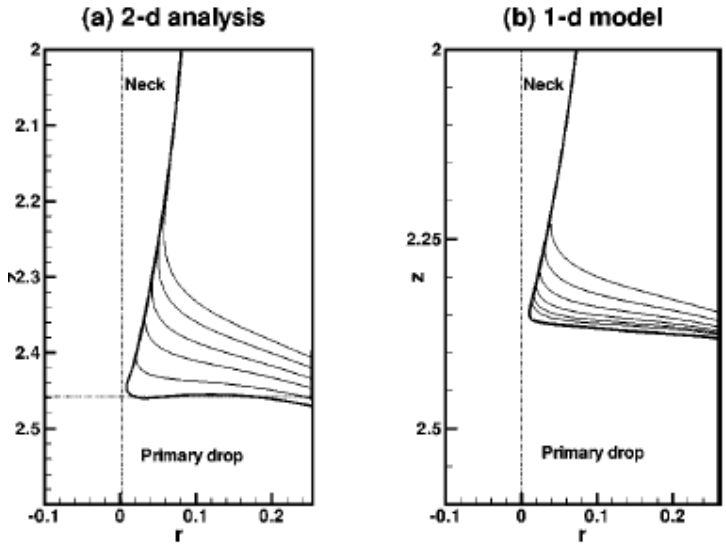

Figure 2.8: Evolution in time of the shapes of a water drop

Comparison of the predicted shapes of drops calculated from 1D models with those from the experiments measured by Brenner et al. [17] shows difference of more than 30% at the time of breakup. [38]

2.2.2.2 Boundary Element/Boundary Integral Method

Schulkes [40] used the boundary element/boundary integral method (BE/BIM) to study the dynamics of drop formation by assuming that the liquid was inciscid and the flow was irrotational. He was able to calculate the first break of the interface, the recoiling

of the thread and the formation of satellite. With BE/BIM, Zhang and Stone [41] investigate the opposite extreme of Stokes flow with the consideration of the effect that the normal and tangential viscous stresses, in addition to pressure, on the drop formation dynamics. However, BE/BIM is restricted to either (i) irrotational flow inside an inviscid drop or (ii) Stokes flow. The Reynolds number is neither zero nor infinite in many applications; so the full Navier-Stokes equations must be solved to quantitatively predict the drop breakup dynamics.

2.2.2.3 Finite Element Method

Finite Element Method (FEM), which is typically not used in solving free surface flows with breakup, is recognized to be a technique of high accuracy in solving steady free surface flows. FEM have been very successful in analysis of steady free surface flows using algebraic mesh generation with spine parametrization of free surfaces and elliptic mesh generation. Wilkes et al. [38] chose FEM to compute the dynamics of drop formation. The computational results have shown that this algorithm is able to compute over the entire range of Re of interest and predict occurrence of microthreads during formation of drops of high-viscosity liquids. FEM have also been used in analysis of liquid drops among others. [42-44] However, the representations for the interface shape in these works, which are radially spherical ray, would fail long before a thin neck would form because a spherical ray would intersect the surface of a deformed drop in more than one location along it.

2.2.2.4 VOF

The techniques which are used to tackle the free surface flows in 2- and 3 dimensions can be classified as Lagrangian, Eulerian, and mixed Lagrangian-Eulerian. [45-48] The Eulerian approach, including volume tracking, such as Volume of Fluid (VOF) method, or surface tracking [49] has been widely used in solving free surface flow problems involving interface rupture.

Hirt et al. [50] first developed the fractional volume of fluid (VOF) method. In general, it is recognized that VOF method is more useful and efficient than other methods for treating complicated arbitrary free boundaries or boundary interfaces. Richards et al. [51] developed a numerical simulation method based on the VOF/CSF technique to investigate the dynamics of liquid drop and formation process from startup to breakup. Their works [51-53] are able to clearly identify the transition from dripping to jetting of the liquid when the liquid flow rate exceeds a critical value. Their numerical simulation results have shown greater accuracy than previously simplified analyses in prediction of jet evolution, velocity distribution and volume of breakoff drops. This technique is capable of predicting the breaking of drops and their coalescence. However, they do not show the kind of accuracy that is required for the microscopic details.

The VOF method differs somewhat from its predecessors like 1D model or BEM/BIM, in two respects. [50-53] Firstly, it uses information about the slope of the surface to

improve the fluxing algorithm. Secondly, the F function is used to define a surface location and orientation for the application of various kinds of boundary conditions, including surface tension forces.

In summary, the VOF method offers a region-following scheme with minimum storage requirements. Furthermore, because it follows regions rather than surfaces, all the problems associated with intersecting surfaces are avoided with the VOF technique. The method is also applicable to three-dimensional computations, where its conservative use of stored information is highly advantageous.

2.3 Analysis of Pressure and Velocity inside Tube

A numerical method of drop formation based on the axisymmetric Navier-Stokes equations was developed by Fromm[54]. He investigated the influence of fluid properties on the flow behaviour based on idealized square pressure histories is unrealistic. Adams and Roy [55] showed that the use of pressure histories is not realistic according to calculation of Fromm's driving pressure formulas, due to the large step change in pressure gradient with time at point.

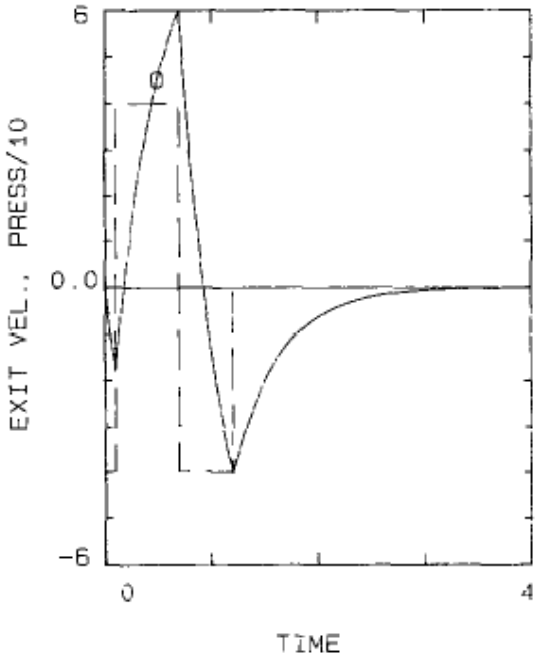

Figure 2.9: Calculated results of velocity at the nozzle region

Bogy and Talke [56] first performed the study of the wave propagation phenomena in drop-on-demand (DOD) inkjet devices by 1D wave equation. The pressure waves were activated by displacement of a cylindrical glass tube arising from the expansion and contraction of a piezoelectric actuator around it. Shield et al. [57] applied the boundary conditions generated in the same manner as Bogy's. The boundary conditions were simply assumed to be zero pressure at the open end with zero velocity at the closed end. As shown in Figure 2.9, the solid line is the nozzle exit velocity, and the dashed line is the step pressure history. Wu et al. [58] [59] employed the same theory as Bogy's of pressure histories to derive the three-dimensional simulation system to describe the drop formation, ejection and impact.

Another numerical method of calculation of the pressure histories at the nozzle is to use inviscid compressible flow theory. Shield et al. [60] first developed this method and solved the 1D wave equations by the characteristic method, which is a technique for solving partial differential equations, to obtain the transient pressure and velocity variations. Chen et al. [61] applied this method into the numerical simulation of droplet ejection process of a piezo-diaphragm printhead instead of the piezo-actuated tube. However, he did not take the surface tension effect into account.

Based on piezoelectricity theory, Bugdayci et al. [62] used the axisymmetric quasistatic solution for the radial motion of piezoelectric actuator as a function of voltage and fluid pressure. But this method did not include the propagation of pressure waves in the axial direction. Wallace et al. [63] determined a formula based on acoustic resonance for the speed of sound in various liquids by taking into consideration the compliance of the piezoelectric tube.

One of the most notable analytical approach of analysing the pressure wave propagation and velocity variation in a small tubular pump was presented by Dijksman [64]. The applied voltage signal was decomposed into a set of sinusoidal waves by Fourier series. Shin et al. [65-67] further developed this method and improved some aspects, in terms of the selection of the number of discrete segments of the taper part (Figure 2.10), the influence of the pressure loading inside the chamber, and the use of thick wall because the wall is assumed to be rigid to simplify the situation.

However, some aspects of this method need to be further understood.

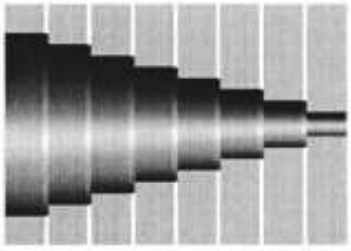

Figure 2.10: Nozzle sectioning

2.4 Conclusion

The research reported in this thesis aims to analyze fluid motion inside a tube. The focus was on the tapered part of nozzle. Thus far, reported methods did not clearly identify nor determine the relationship between the actuated, unactuated, and taper segments of the nozzle. In addition, the upstream boundary condition has been assumed to be a semi-infinite channel in the form of $C \cdot \exp(\psi z)$ when the radius of the connecting tube is similar to that of the inlet tube of the printhead. But in reality, there is a negative pressure, which is called “back pressure”, to hold the fluid inside the chamber to prevent it flowing outside continuously. Furthermore, the study regarding the number of Fourier terms has not been done, although it significantly affects the computing time.

The simulating modeling presented in this thesis is based on 2D VOF method for Newtonian fluid. The reason is that although the 1D model has made contribution for our understanding of dynamics of drop formation, they have not been able to capture

both the macroscopic features, such as the size of the primary drop, and the time to breakup at any value of the flow rate, and the microscopic features, such as the length of the main thread. We employ Newtonian fluid in our study for simplification, because several factors have to be considered in non-Newtonian fluid, such as oscillatory shear, or rheological properties.

Chapter 3 Related Issues of Modeling and Simulation

One of the most important issues of modeling and simulation of drop formation from a nozzle is the analysis of the fluid behavior inside the channel induced by the radial motion of the piezoelectric tube. This analysis yields the pressure or axial velocity history at the nozzle, which is used as the pressure or velocity boundary condition for the modeling of the drop formation process.

Another issue is the pulse voltage which is used to activate the piezoelectric tube. In the analytical approach, the pulse voltage is decomposed into a set of sinusoidal waves over the time using the Fourier series. The study regarding to the number of Fourier terms has not been done, although it significantly affects the computing time. The considerate number of Fourier terms is found in this chapter.

3.1 Analysis of the Fluid Behavior inside Channel

Numerous notable works about modeling of drop formation from a nozzle have been carried out, but the fluid motion in the ink flow channel receives less attention from the investigators. Some pioneer researches have been done as described in chapter 2. Nevertheless, some aspects of the analytical method need to be further understood. Firstly, the focus was on the taper part of nozzle, but did not clearly explain the relationship between the actuated, unactuated and taper parts. Secondly, the upstream

boundary condition was assumed to be a semi-infinite channel in the form of $C \cdot \exp(\psi z)$ when the radius of the connecting tube is similar to that of the inlet tube of printhead. However, in reality, there is a negative pressure, which is called “back pressure” to hold the fluid inside the chamber to prevent it flowing outside continuously.

This section aims to achieve the following: implementing a realistic upstream boundary condition rather assuming zero pressure on the inlet in the case that the radius of reservoir is much larger than that of inlet tube; solving the equations with the appropriate boundary conditions for each part.

3.1.1 Mathematical Formulation

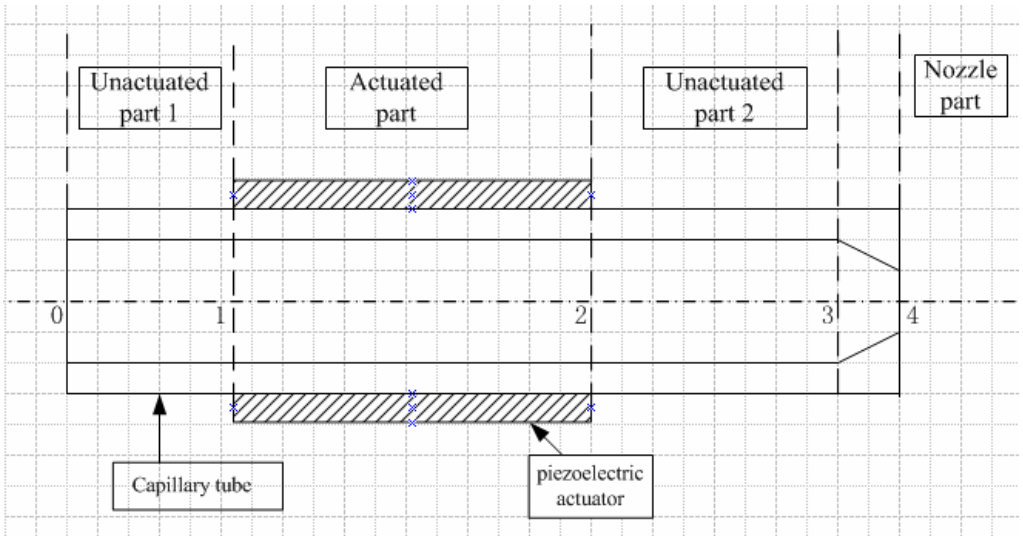

Figure 3.1: Schematic of inkjet printing head

In this section, the functions of calculating the pressure and axial velocity for the fluid flow at each part are introduced and all the unknown coefficients in the functions are solved by combining with appropriate boundary conditions. As shown in Figure 3.1, the printhead is divided into four parts: unactuated part1 (without connecting with the nozzle part), actuated part, unactuated part 2 (connected with the actuated part and the nozzle part) and nozzle part.

The derivation of the analytical solutions for pressure and velocity at actuator and nozzle part has been done by Shin et al. [65] [66]. The downstream pressure boundary condition derived by Shin [66] [67] based to the membrane theory is also adopted in this model. Here the derivation of the functions of pressure and velocity for unactuated parts is exhibited for the first time and the upstream pressure boundary condition is applied with a newly realistic back pressure instead of semi-infinite channel condition. The four groups of pressure and velocity equations are solved together with boundary conditions to obtain the final exit velocity history for simulation purpose.

3.1.1.1 Formulation for Each Part

The governing equations are Navier-Strokes equations and mass continuity. Only the mass continuity and r and z momentum equations maintain for the reason that the fluid flow in an elastic tube is assumed to be axisymmetric and laminar flow, the θ momentum equation can be ignored.

The assumptions made are as following: (1) fluid flow inside the channel is regarded as incompressible flow, (2) since the pressure gradient in the r direction is much smaller than that in z direction, the pressure is assumed to be a z dependent function, (3) the z momentum Navier-Strokes equation is linearized, so the convective acceleration terms are ignored. The time dependence, $e^{i\omega t}$, is omitted in all equations for convenience, where i and ω are the imaginary number and angular frequency, respectively.

Derivation of functions for unactuated part1

According to the radial stress boundary conditions at inner and outer of glass tube part without actuator [65], the radial stress at inner and outer of the glass tube are:

$$\sigma_r^C|_{r1} = C_3 f + C_4 \frac{g}{r_1^2} = -P(z) \tag{3.1}$$

$$\sigma_r^C|_{r2} = C_3 f + C_4 \frac{g}{r_2^2} = 0 \tag{3.2}$$

Through (3.1) and (3.2), the explicit expressions of C_3 and C_4 are obtained.

$$C_3 = \frac{P(z) r_2^2}{f(r_2^2 - r_1^2)}, \quad C_4 = \frac{-P(z) r_1^2 r_2^2}{g(r_2^2 - r_1^2)}$$

After substituting the expressions of C_3 and C_4, and rearranging it, the radial displacement at inner of the glass tube is achieved.

$$u^C(r_1, z) = \frac{(g - f) r_1 r_2^2}{fg(r_2^2 - r_1^2)} P(z)$$

Compare to the function of radial displacement of glass tube for actuated part, the new coefficient A is defined.

$$A=\frac{(g-f)r_1r_2^2}{fg(r_2^2-r_1^2)},\quad g=-\frac{E_C}{1+\nu_C},\quad f=\frac{E_C}{(1+\nu_C)(1-2\nu_C)}$$

So the function of the radial displacement at inner of the glass tube for unactuated part is

$$u^C(r_1,z)=A\cdot P(z)$$

And the functions of pressure and velocity of fluid inside the unactued glass tube which is not connected with nozzle are also obtained.

Unactuated part1 (without connection with nozzle):

$$P(z)=C_5\exp(\psi' z)+C_6\exp(-\psi' z) \tag{3.3}$$

$$V_z(r,z)=\frac{\psi'}{-\rho_f i\omega}\left(1-\frac{J_0(\lambda r)}{J_0(\lambda r_1)}\right)\{C_5\exp(\psi' z)-C_6\exp(-\psi' z)\} \tag{3.4}$$

where $\psi'=\sqrt{\frac{\beta'}{\alpha}}$, $\beta'=-(2\pi r_1 i\omega A+\frac{i\omega\pi r_1^2}{\rho_f c_f{}^2})$, $\alpha=\frac{\pi}{\rho_f i\omega}\left(r_1^2-\frac{2r_1J_0(\lambda r_1)}{\lambda J_0(\lambda r_1)}\right)$,

$\lambda=\sqrt{-\frac{i\omega}{\nu_f}}$,

The functions at unactuated part2 are similar to those at unactuated part1. The only difference is the unknown coefficients, which are represented as C_3 and C_4, for taking account of the influence of the fluid movement at different positions.

Actuated part:

$$P(z)=C_1\exp(\psi z)+C_2\exp(-\psi z)+\gamma \tag{3.5}$$

$$V_z(r,z)=\frac{\psi}{-\rho_f i\omega}\left(1-\frac{J_0(\lambda r)}{J_0(\lambda r_1)}\right)\{C_1\exp(\psi z)-C_2\exp(-\psi z)\} \tag{3.6}$$

Nozzle part:

$$P(z) = C_7 + C_8 \int \exp^{(\int F_3(z)dz)} dz \tag{3.7}$$

$$V_z(r,z) = \frac{\psi}{-\rho_f i\omega}\left(1 - \frac{J_0(\lambda r)}{J_0(\lambda r_4(z))}\right) C_8 \exp^{(\int F_3(z)dz)} \tag{3.8}$$

where $F_1(z) = \int_0^{r_4(z)} r - \frac{rJ_0(\lambda r)}{J_0(\lambda r_4(z))} dr$, $F_2(z) = \int_0^{r_4(z)} rJ_0(\lambda r)dr \frac{\lambda \tan(\theta) J_1(\lambda r_4(z))}{J_0(\lambda r_4(z))^2}$

$F_3(z) = \frac{F_1(z)}{F_2(z)}$, C_1, C_2, C_7 and C_8 are unknown coefficients.

3.1.1.2 Pressure Boundary Conditions

Downstream pressure boundary condition

In the early studies, the common treatment for the downstream boundary condition was imposing the ambient pressure, which means zero pressure difference at the outlet of print head [56-59] [64]. Shin [66] [67] developed a reasonable condition according to the membrane theory based on the fact that the axial velocity acceleration due to the high capillary pressure. It is adopted here.

$$\Delta P = C_8 F_2 \left\{ -\frac{2\sigma_f \lambda}{\rho_f \omega^2 \lambda r_0} \frac{J_1(\lambda r_0)}{J_0(\lambda r_0)} + \frac{4\mu_f}{\rho_f i\omega {r_0}^2} \left(\frac{{r_0}^2}{2} - \frac{r_0 J_1(\lambda r_0)}{\lambda J_0(\lambda r_0)} \right) F_1 - \frac{4\mu_f}{\rho_f i\omega {r_0}^2} \frac{\tan(\theta) r_0 J_1(\lambda r_0)}{J_0(\lambda r_0)^2} \right\}$$

(3.9)

where $\triangle P$, σ_f, μ_f and r_0 represent pressure difference, surface tension, dynamics viscosity and nozzle orifice radius, respectively. Eq. (3.9) shows the average pressure along the membrane surface.

Upstream pressure boundary condition

There are two kinds of solutions for the upstream pressure boundary condition. One is the usual zero pressure for simplicity [56] [57], if the radius of the reservoir connected to the inkjet print head, is much larger than that of inlet tube. The length becomes $l_i + 0.82 \times r_i$, with the representation that l_i and r_i are the length and the radius of the glass tube. The other solution is regarding the tube as a semi-infinite tube when the radius of the inlet is similar to that of the connecting tube of the reservoir, and equals to $C \cdot \exp(\psi z)$ for making the pressure and velocity decay from the inlet towards reservoir, where C is an arbitrary constant [56] [57].

In our case there is a negative pressure applied by the pressure controller at the reservoir end, which is used to hold the fluid inside the tube and prevent it flowing downside continuously. Hence, the upstream pressure boundary condition cannot be defined as ambient pressure or zero pressure at the inlet of the capillary tube, although the radius of the reservoir is much larger than that of the inlet tube. It is sensible to employ the Eq.(3.10) as the upstream boundary condition, where P_0 is the negative pressure.

$$P_0 = C_5 \exp(\psi' z) + C_6 \exp(-\psi' z) \qquad (3.10)$$

3.1.2 Solving Equations

Our aim is to obtain the exact axial velocity function with respect to time at the nozzle orifice. There are 8 unknown coefficients, so it needs 8 equations to be solved to get them. At point 0 and 4, Eq.(3.10) and (3.17) are obtained by applying the upstream

and downstream boundary conditions. Other equations are determined by applying the continuity of pressure and mass flow for each equation at adjacent boundary. The continuity of mass flow is becoming that of velocity with the condition of the same cross section area at the same point. Hence, at each point of 1, 2 and 3, one pressure equation and one velocity equation will be obtained, respectively.

P0: $P_0 = C_5 \exp(\psi' z) + C_6 \exp(-\psi' z)$ (3.10)

P1: $C_5 \exp(\psi' z) + C_6 \exp(-\psi' z) = C_1 \exp(\psi z) + C_2 \exp(-\psi z) + \gamma$ (3.11)

$$\frac{\psi'}{-\rho_f i\omega}\left(1-\frac{J_0(\lambda r)}{J_0(\lambda r_1)}\right)\{C_5 \exp(\psi' z) - C_6 \exp(-\psi' z)\} = \frac{\psi}{-\rho_f i\omega}\left(1-\frac{J_0(\lambda r)}{J_0(\lambda r_1)}\right)\{C_1 \exp(\psi z) - C_2 \exp(-\psi z)\} \quad (3.12)$$

P2: $C_3 \exp(\psi' z) + C_4 \exp(-\psi' z) = C_1 \exp(\psi z) + C_2 \exp(-\psi z) + \gamma$ (3.13)

$$\frac{\psi}{-\rho_f i\omega}\left(1-\frac{J_0(\lambda r)}{J_0(\lambda r_1)}\right)\{C_1 \exp(\psi z) - C_2 \exp(-\psi z)\} = \frac{\psi'}{-\rho_f i\omega}\left(1-\frac{J_0(\lambda r)}{J_0(\lambda r_1)}\right)\{C_3 \exp(\psi' z) - C_4 \exp(-\psi' z)\} \quad (3.14)$$

P3: $C_3 \exp(\psi' z) + C_4 \exp(-\psi' z) = C_7 + C_8 \int \exp^{(\int F_3(z)dz)}\, dz$ (3.15)

$$\frac{\psi'}{-\rho_f i\omega}\left(1-\frac{J_0(\lambda r)}{J_0(\lambda r_1)}\right)\{C_3 \exp(\psi' z) - C_4 \exp(-\psi' z)\} = \frac{\psi}{-\rho_f i\omega}\left(1-\frac{J_0(\lambda r)}{J_0(\lambda r_4(z))}\right) C_8 \exp^{(\int F_3(z)dz)} \quad (3.16)$$

$$\text{P4:}\quad C_7 + C_8 \int \exp^{(\int F_3(z)dz)}\, dz = \Delta P + P_a \tag{3.17}$$

P_a is ambient pressure. All the calculation of the above equations is executed in MAPLE.

3.1.3 Final Pressure and Velocity Functions

The functions of pressure and velocity in the dime domain are discovered by Fourier analysis. The time dependent item, $\exp(i\omega t)$, is omitted in all the equations for the convenience. In order to avoid misunderstanding in use of these functions, the complete explicit functions of pressure and velocity are exhibited here. The final pressure and velocity functions at nozzle part are:

$$P(z,t) = \sum_{\omega}\left(C_7 + C_8 \int \exp^{(\int F_3(z)dz)}\, dz \right) \cdot \exp(i\omega t) \tag{3.18}$$

$$V_z(r,z,t) = \sum_{\omega}\left(\frac{\psi}{-\rho_f i\omega}\left(1 - \frac{J_0(\lambda r)}{J_0(\lambda r_4(z))}\right) C_8 \exp^{(\int F_3(z)dz)} \right) \cdot \exp(i\omega t) \tag{3.19}$$

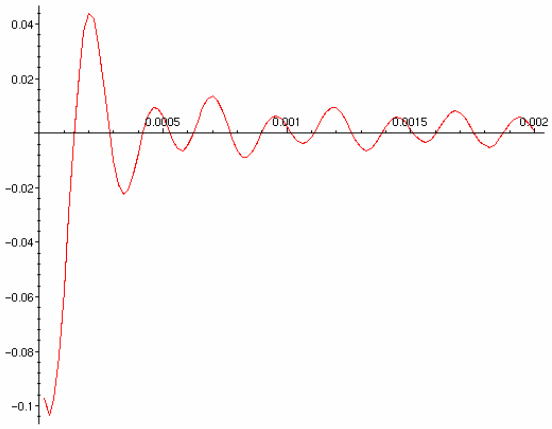

Figure 3.2: Axial velocity history at the nozzle exit

The axial velocity history at the nozzle exit is computed according to Eq.(3.12) with 40 Fourier terms and the result is plotted in Figure 3.2. As shown, the velocity history is not a monotone function as imagined, but a kind of oscillatory function in time domain, which is in the similar form as Shin [67]. The possible reason is the interaction between the back pressure and the pressure wave inside the glass tube produced by the periodic motion of piezoelectric actuator.

3.2 Pulse Voltage

3.2.1 Pulse Waveform

There are two kinds of waveform that we usually use to move the piezoelectric transducer in the inkjet printing. One waveform is so-called uni-polar pulse wave which is trapezoidal, as shown in Figure 3.3. Another one is bipolar pulse wave in Figure 3.4. The function of the initial portion of the bipolar waveform remains the same as uni-polar. The second part of waveform is used to cancel some of the residual acoustic oscillations remaining in the device.

Based on previous work, for a uni-polar pulse wave, good droplet dispensing can be achieved by setting the rise time (t_{rise}) and fall time (t_{fall}) to 3μs, the Dwell time (t_{dwell}) and Pulse amplitude (V) are identified as significant factors in affecting drop formation, hence these parameters will be varied and their effects on velocity and volume investigated.

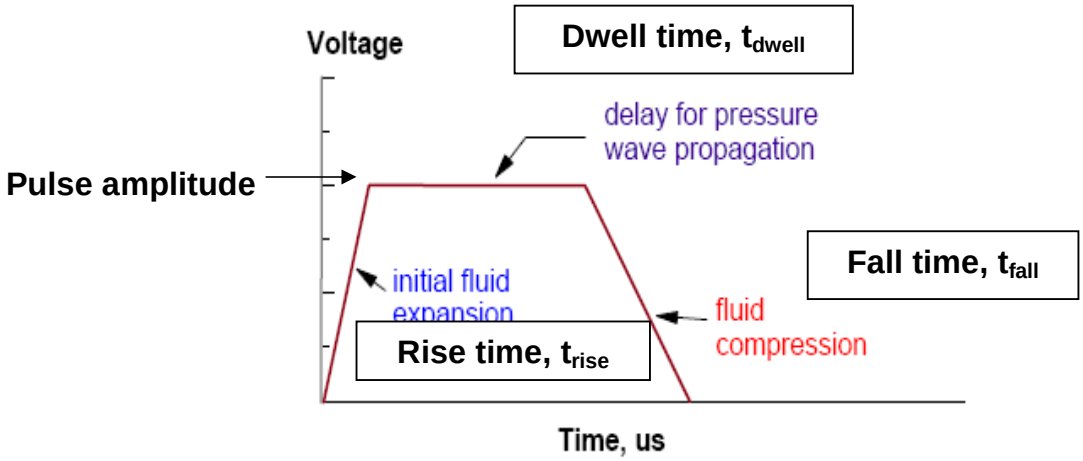

Figure 3.3: Uni-Polar Pulse Wave

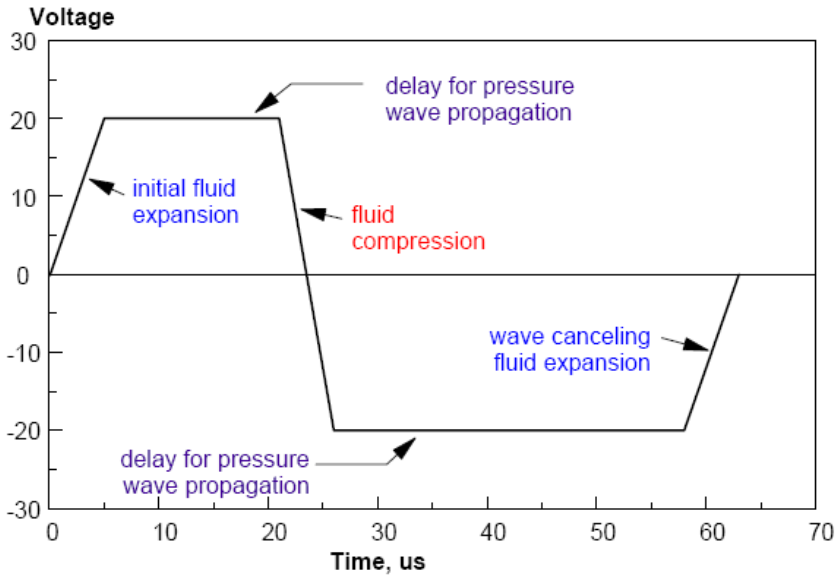

Figure 3.4: Bipolar Pulse Wave

3.2.2 Fourier series Analysis

The occurrence of the exponential item $\exp(i\omega t)$ with imaginary number i and angular frequency ω, results from solving equation by the method of separation of variables [64]. As the governing equations are linearized, the response in time domain is determined by Fourier series analysis. The applied voltage waveform in the time domain is decomposed into a set of sinusoidal function in the frequency domain. The final resultant velocity is the sum of the velocity from each Fourier series component. The decomposition of the applied voltage waveform can be performed in MAPLE. Here is the program in MAPLE for decomposition of the applied voltage.

```
flyc := proc(f,mg::(name = range),n::posint)
local a, b, T, z, sum, k;
a := lhs(rhs(mg));
b := rhs(rhs(mg));
T := b–a;
z := 2* π *t/T;
sum := int(f, mg)/T;
for k to n do sum := sum + algsubs( cos(k*z)=1/2*exp(–I*z*k)+1/2*exp(I*z*k),
algsubs( sin(k*z)=1/2*I*(exp(–I*z*k)– exp(I*z*k)),
2*int(f*cos(k*z),mg)*cos(k*z)/T+2*int(f*sin(k*z),mg)*sin(k*z)/T) )
od;
[algsubs(2* π / T = w0, sum),"w0=",z/t,"N=",n]
```

end;

3.2.3 The Number of Fourier series Terms

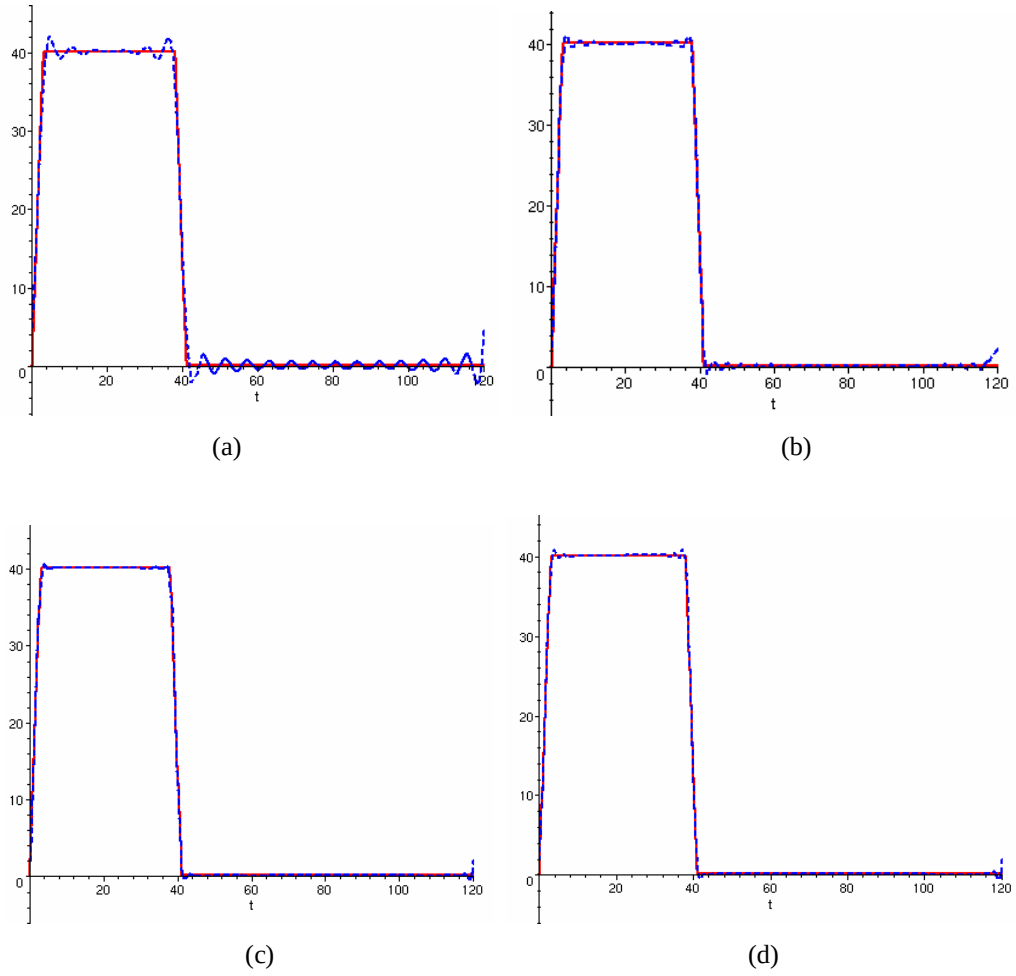

Figure 3.5: Fourier series approximated voltage waveform for 40V with different number of terms (a) 20. (b) 30. (c) 40. (d) 50.

The trapezoidal voltage function in the time domain is decomposed into a set of sinusoidal functions in the frequency domain with the Fourier series. As shown in Figure 3.5, 40 Fourier terms will be recommended to use.

In (a) the voltage is decomposed with 20 Fourier terms in 141.3s; (b) with 30 Fourier terms in 143.7s; (c) with 40 Fourier terms in 221.9s; (d) with 50 Fourier terms in 281.5s. The percentage errors are 4.525%, 2.075%, 1.125% and 1.425% for case (a-d), respectively. From the data above, 40 Fourier terms would be sufficient to describe the given waveform with the less time taken than 50 terms.

Chapter 4 Simulation and Modeling of Drop Formation from Piezo-Actuated Dispenser

The simulation and modeling of the drop formation in the research is carried out using the advanced computational fluid dynamic software, FLUENT and Gambit. Gambit is used to generate the geometry and mesh, which is called the pre-process. FLUENT is used to simulate and model the process of the drop formation. In FLUENT, the method used for the generation and analysis of the drop formation is Volume of Fluid (VOF) method and Piecewise Linear Interface Calculation (PLIC) scheme. The driving signal which is applied to the piezo-actuated capillary is simulated with a fluent-C program using the User Defined Function (UDF) of FLUENT.

4.1 Theory of Drop Formation from Piezo-Actuated Dispenser

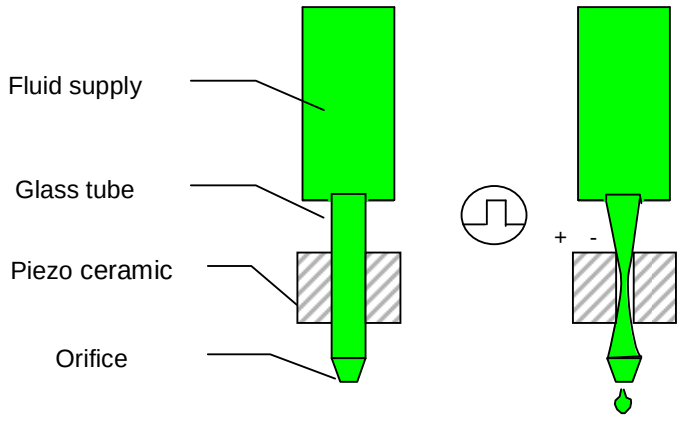

Figure 4.1: Schematic diagram of piezo-dispensing

The axisymmetric formation of drops of Newtonian liquids from a vertical capillary into air is governed by axisymmetric Navier–Stokes equation with appropriate boundary and initial conditions. The boundary condition at the inlet of the nozzle is determined by the propagation of acoustic waves.

As shown in Figure 4.1, the capillary tube, which is provided with electrodes on the Piezo ceramic's inner and outer surfaces, can be polarized radially. When a voltage pulse is applied across the piezoelectric transducer tube, a radial displacement of the tube is initiated. Depending on the polarization of the PZT, the inner radius can increase or decrease with the voltage variation, causing an instantaneous pressure distribution in the cavity. The generated acoustic wave causes a small amount of the liquid to be expelled from the orifice. Due to the pressure pulse some of the fluid is forced back into capillary tube, but the amount is relatively small due to high acoustic impedance created by the length and small bore of the capillary tube. Because of the small rate of change of volume during the decay, the accompanying pressure reduction is too small to overcome the surface tension at the orifice. Consequently the liquid flows into the capillary to replace the liquid previously expelled without drawing in air through the orifice. [37]

4.2 Simulation Methodology

This section describes the VOF interface tracking method that uses a PLIC in each cell. Momentum balance is computed using explicit finite volume/finite differences on

the grid. Surface tension is implemented by the continuous surface stress or continuous surface force method.

4.2.1 Volume of Fluid (VOF) Method

The VOF method consists of three ingredients: a scheme to locate the surface, an algorithm to track the surface as a sharp interface moving through a computational grid, and a means of applying boundary conditions at the surface. It is one of the surface-tracking techniques applied to a fixed Eulerian mesh, designed for two or more immiscible fluids where the position of the interface between the fluids is of interest.

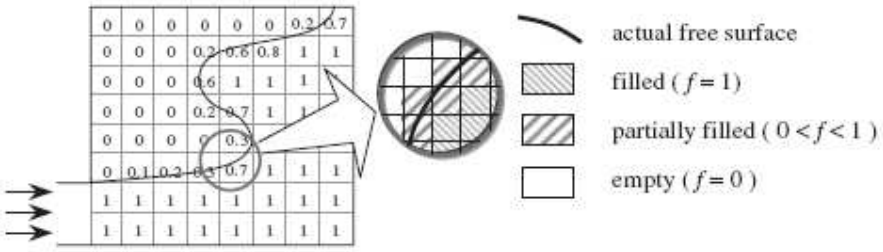

Figure 4.2: VOF method

In the VOF method, fractional fluid volume in a cell (or in a control volume) is used to represent the free surface on the fixed grids. Each rectangle in Figure 4.2 denotes a unit cell. The VOF formulation relies on the face that two or more fluids (or phases) are not interpenetrating. In each computational cell, the volume fraction of all phases sum to unity. All the phases share the fields for all variables and properties. Thus the variables and properties in any cell are either purely representative of one of the phases, or representative of a mixture of the phases. If the qth fluid's volume fraction

in the cell is referred to as α_q, then the following three conditions are possible:

- $\alpha_q = 0$: the cell is empty (of the qth fluid).
- $\alpha_q = 1$: the cell is full (of the qth fluid)
- $0 < \alpha_q < 1$: the cell contains the interface between the qth fluid and one or more other fluids.

A single set of momentum equations is shared by the fluids, and the volume fraction of each of the fluids in each computational cell is tracked throughout the domain such that the volume fractions of all phases sum to unity. The volume fraction is a step function, having a value of either one or zero.[50] In addition, the volume fractions in neighboring cells can then be used to locate the position of fluid (and its slope and curvature) within a particular cell. The surface boundary conditions must be applied by assigning the proper gas pressure (plus equivalent surface tension pressure) as well as determining what velocity components outside the surface should be used to satisfy a zero shear-stress condition at the surface.

Finally, to compute the time evolution of surfaces, a technique is used to move volume fractions through a grid in such a way that the step-function nature of the distribution is retained. The basic kinematic equation for fluid fractions is similar to that for the height-function method, where F is the fraction of fluid function.[71]

$$\frac{\partial F}{\partial t} + u\frac{\partial F}{\partial x} + v\frac{\partial F}{\partial y} + w\frac{\partial F}{\partial z} = 0 \qquad (4.1)$$

The fields for all variables and properties are shared by the phases and represent volume-averaged values, as long as the volume fraction of each of the phases is known at each location. Thus the variables and properties in any given cell are either purely representative of one of the phases, or representative of a mixture of the phases, depending upon the volume fraction values.

4.2.2 Piecewise Linear Interface Calculation (PLIC) Scheme

The aftertreatment VOF method describes the interface implicitly since the volume fraction data must be inverted to find the approximate interface position. The interface may be reconstructed by SLIC (simple line interface calculation) or by various PLIC (piecewise linear interface calculation) scheme. The latter methods give much better results than the former as noted in the review in Chapter two. [68]

In PLIC scheme, at each time step, if the volume fraction of one of the two fluids in each computational cell and an estimate of the normal vector to the interface are known, a planar surface is constructed within the cell having the same normal and dividing the cell into two parts. Each of these two parts contains the proper volume of one of the two fluids. This planar interface is then propagated by the flow, and the resulting volume, mass, and momentum fluxes of each fluid into neighboring cells are determined. The updated values of the volume fraction field, as well as the mass and momentum fields, are found throughout the domain, and the numerical simulation can proceed to the next time step.

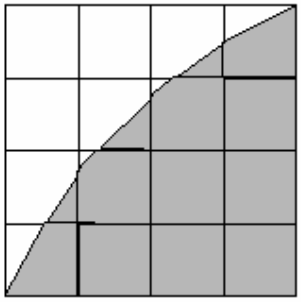

Figure 4.3: Interface shape represented by the geometric reconstruction (PLIC) scheme

In FLUENT, the geometric reconstruction scheme is used to represent the interface between fluids by using a piecewise-linear (PLIC) method. When the computational cell is near the interface between two phases, the geometric reconstruction scheme is implemented. It assumes that the interface between two fluids has a linear slope within each cell, and uses this linear shape for calculation of the advection of fluid through the cell faces. There are three steps in the geometric reconstruction scheme as following [71]:

1) Calculate the position of the linear interface relative to the center of each partially-filled cell, based on information about the volume fraction and its derivatives in the cell.

2) Calculate the advecting amount of fluid through each face using the computed linear interface representation and information about the normal and tangential velocity distribution on the face.

3) Calculate the volume fraction in each cell using the balance of fluxes calculated during the previous step.

4.2.3 Continuous Surface Force (CSF) Method

The surface tension model in FLUENT is the continuum surface force (CSF) model proposed by Brackbill et al. [69] With this model, the addition of surface tension to the VOF calculation results in a source term in the momentum equation.

In CFS model, interfaces between fluids of different properties are assumed as transition regions of finite thickness. At each point in the transition region, a force density is defined which is proportional to the curvature of the surface of constant fluid at that point. The surface tension is treated as a continuous, three-dimensional effect across an interface, rather than a boundary value condition on the interface.

In CSF formulation, discontinuities can be approximated without increasing the overall error of approximation, as continuous transitions within which the fluid properties vary smoothly from one fluid to the other over a distance of O(h), where O is a distance function for the transition region, and h is a width of the transition region. Therefore, surface tension exists everywhere within the transition region through the volume force included in the momentum equations. The surface force in the momentum equation is

$$F_{SV} = \sigma \kappa n \qquad (4.2)$$

where κ is the curvature of the liquid-liquid interface, n is the surface normal vector.

The CSF method is capable of using the smoothed VOF function $F_{i,j}$ for the calculation of the curvature $\kappa_{i,j}$ in the volume force Eq. (4.2). This enables the algorithm to calculate a smoother curvature, giving improved accuracy. The CSF method also eliminates the need for interface reconstruction, simplifies the calculation of surface tension of two- and three-dimensional fluid flows driven by surface tension.

4.2.4 Time Dependence

For time-dependent VOF calculations, the momentum equation is solved using an explicit time-marching scheme. The time step used for the volume fraction calculation will not be same as the time step used for the rest of the transport equations. FLUENT refines the time step for the integration of the volume fraction equation automatically, but this time step calculation can be influenced by modifying the Courant number. You can choose to update the volume fraction once for each time step, or once for each iteration within each time step.

The Courant number is a dimensionless number that compares the time step in a calculation to the characteristic time of transit of a fluid element across a control volume, which is defined as:

$$\frac{\Delta t}{\Delta x_{cell} / v_{fluid}} \qquad (4.3)$$

4.3 Mathematic Formulation

4.3.1 Volume Fraction Equation

The solution of a continuity equation for the volume fraction of two of the phases is used to track the interface between the phases. For the qth phase, this equation has the following form [73]:

$$\frac{1}{\rho_q}\left[\frac{\partial}{\partial t}(\alpha_q\rho_q)+\nabla\cdot(\alpha_q\rho_q\vec{v}_q)=S_{\alpha_q}+\sum_{p=1}^{n}(\dot{m}_{pq}-\dot{m}_{qp})\right] \qquad (4.4)$$

where $\dot{m}_{qp}$ is the mass transfer from phase q to phase p and $\dot{m}_{pq}$ is the mass transfer from phase p to phase q. By default, the source term on the right-hand side of Eq. (4.4) S_{α_q}, is zero.

The volume fraction equation will not be solved for the primary phase; the primary-phase volume fraction will be computed based on the following constraint:

$$\sum_{q=1}^{n}\alpha_q=1 \qquad (4.5)$$

4.3.2 Properties

The properties are determined by the component phases in each control volume. If the phases are represented by the subscripts air=1 and material=2, and if the volume fraction of the second material of these is being tracked, the density in each cell is denoted by [73]:

$$\rho=\alpha_2\rho_2+(1-\alpha_2)\rho_1 \qquad (3.6)$$

4.3.3 Momentum Equation

A single momentum equation, [73] which is dependent on the volume fraction of all phases through the properties of density and viscosity, is solved throughout the domain, and the resulting velocity field is shared among the phases.

$$\frac{\partial}{\partial t}(\rho\vec{v})+\nabla\cdot(\rho\vec{v}\vec{v})=-\nabla\cdot\left[\mu(\nabla\vec{v}+\nabla\vec{v}^{T})\right]+\rho\vec{g}+\vec{F} \qquad (4.7)$$

4.3.4 Energy Equation

The energy equation is shown below [73]:

$$\frac{\partial}{\partial t}(\rho E)+\nabla\cdot(\vec{v}(\rho E+p))=\nabla\cdot(\kappa_{eff}\nabla T)+S_h \qquad (4.8)$$

The VOF model treats energy, E as mass-averaged variables:

$$E=\frac{\sum_{q=1}^{n}\alpha_q p_q E_q}{\sum_{q=1}^{n}\alpha_q p_q} \qquad (4.9)$$

where E_q for each phase is based on the specific heat of that phase and the shared temperature.

4.3.5 Surface Tension

In FLUENT, the CSF model is used to formulate the surface tension. The surface curvature is computed form local gradients in the surface nomal at the interface. The surface normal is denoted by n, and defined as the gradient of the volume fraction of the qth phase:

$$n=\nabla\alpha_q \qquad (4.10)$$

The curvature κ, is defined in terms of the divergence of the unit normal $\hat{n}$:

$$\kappa = \nabla \cdot \hat{n} \qquad (4.11)$$

where $\hat{n} = \frac{n}{|n|}$ (4.12)

The surface tension can be written in terms of the pressure jump across the surface. The force at the surface can be expressed as a volume force using the divergence theorem. It has the following form:

$$F_{vol} = \sigma_{ij} \frac{\rho \kappa_i \nabla \alpha_i}{\frac{1}{2}(\rho_i + \rho_j)} \qquad (4.13)$$

where σ is the surface tension coefficient.

4.4 Solution

4.4.1 Basic Linearization Principle

In FLUENT, Non-linear governing equations are linearized to produce a system of equations for the dependent variables in every computational cell. The resultant linearized system is then solved to obtain an updated flow-field solution. The unknown variables in each cell are computed using a relation that includes both existing and unknown values from neighboring cells. Therefore each unknown will appear in more than one equation in the system, and these equations must be solved simultaneously to give the unknown quantities.

4.4.2 Segregated Solution Method

The segregated solver is the solution algorithm previously used by FLUENT, which is

used to solve the governing equations for the conservation of mass and momentum. Because the governing equations are non-linear, several iterations of the solution loop must be performed before a converged solution is obtained. Each iteration consists of the steps illustrated in Figure 4.4 [73] and outlined below:

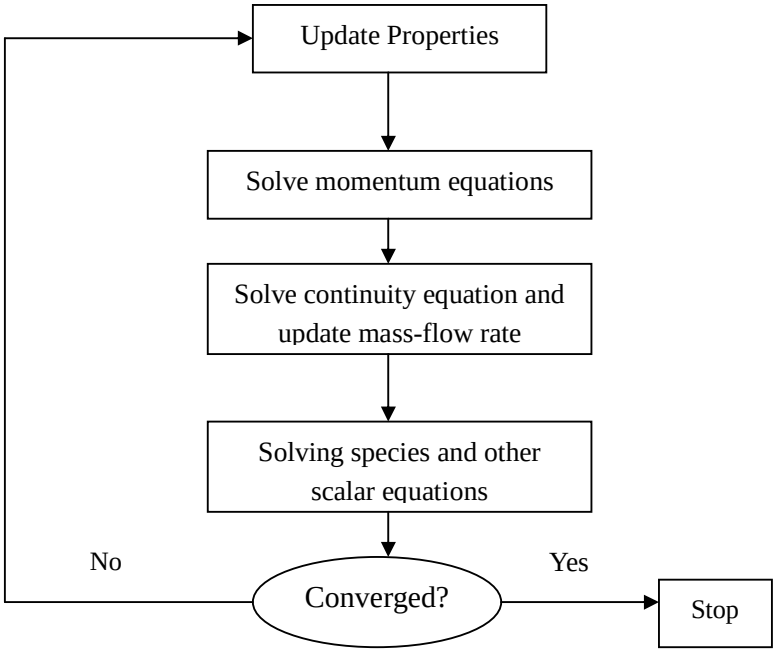

Figure 4.4: General solving sequence

1. Fluid properties are updated, based on the current solution. (If the calculation has just begun, the fluid properties will be updated based on the initialized solution.)

2. The u, v, and w momentum equations are each solved in turn using current values for pressure and face mass fluxes, in order to update the velocity field.

3. Since the velocities obtained in Step 2 may not satisfy the continuity equation locally, a “Poisson-type” equation for the pressure correction is derived from the continuity equation and the linearized momentum equations. This pressure

correction equation is then solved to obtain the necessary corrections to the pressure and velocity fields and the face mass fluxes such that continuity is satisfied.

4. Where appropriate, equations for scalars such as turbulence, energy, species, and radiation are solved using the previously updated values of the other variables.

5. When interphase coupling is to be included, the source terms in the appropriate continuous phase equations may be updated with a discrete phase trajectory calculation.

6. A check for convergence of the equation set is made.

These steps are continued until the convergence criteria are met.

In segregated method, each discrete governing equation is linearized implicitly with respect to that equation's dependent variable. This will cause a system of linear equations with one equation for each cell in the domain. Because there is only one equation per cell, this is sometimes called a “scalar" system of equations. A point implicit (Gauss-Seidel) linear equation solver is used in conjunction with an algebraic multigrid (AMG) method to solve the resultant scalar system of equations for the dependent variable in each cell. Simultaneous solution of this equation system (using the scalar AMG solver) yields an updated u-velocity field.

In conclusion, the segregated approach solves for a single variable field (e.g. velocity) by considering all cells at the same time. It then solves for the next variable field by again considering all cells at the same time, and so on. There is no explicit option for

the segregated solver.

4.5 Simulating and Modeling

4.5.1 Computational Mesh

The computational mesh for modeling of drop formation is generated by using the software Gambit. Because the simulation is carried out in two-dimension, this computational mesh is created for the axis-symmetric 2D. It has the following boundary regions.

1. Nozzle-outlet (velocity inlet): The Velocity Inlet sets the boundary conditions for a velocity inlet zone, which is the nozzle outlet. The inflow velocity can be defined by specifying the velocity magnitude and direction, the velocity components, or the velocity magnitude normal to the boundary. Here the velocity is applied normal to the boundary under consideration as velocity inlet. The velocity magnitude applied is a user defined program, which is computed by the axial velocity history at the nozzle (see details in Chapter 3).
2. Wall: wall boundary condition is used to bound fluid and solid regions. Here the wall boundary condition for this region of the panel is set as stationary wall.
3. Pressure outlet: the boundary condition at the section parallel to the axis is set as pressure outlet, which signifies that the atmospheric pressure acts on the drop and the gauge pressure is set to zero and the backward flow is set

as normal to the pressure outlet section.

4. Outflow: the outflow is set to the section parallel to the velocity inlet zone, indicating as the direction in which the drop is going to travel after it gets pinched off from the orifice nozzle.
5. Axis-symmetric (axis): here the modeling and analysis is done by considering only right half of the drop along its axis. And this axis-symmetric is set to the zone as shown in Figure 4.5.

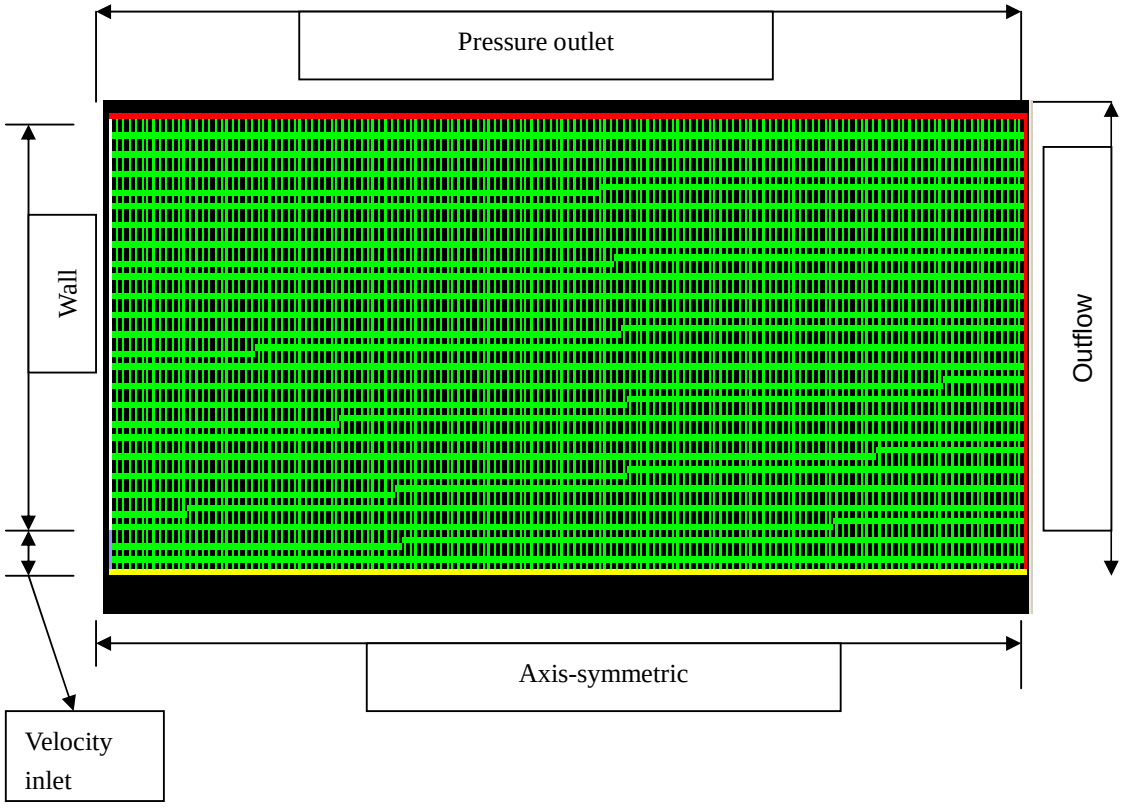

Figure 4.5: Computational mesh created with Gambit

The scaling of the grid is done and scaling is (0, 0) to (0.25, 1.5) and the velocity inlet is (0, 0) to (0, 0.025). All the units are in “mm”.

Table 4.1: dimensioning of mesh

NAME	Mesh Dimension
Velocity inlet	0.025mm
Axis-symmetric	1.5mm
Outflow	0.25mm
Pressure out	1.5mm
Wall	0.225mm

4.5.2 Velocity Calculated by UDF

In order to apply the calculated velocity history at the nozzle into the model of drop formation, FLUENT provides a user-defined function (UDF), which is a function that the program can be dynamically loaded with the FLUENT solver. UDFs are written in the C programming language. They access data from the FLUENT solver using predefined macros and functions supplied by Fluent Inc.

There are two kinds of ways for application of velocity history through UDF. One approach is using UDF to read the data from the text file. Another one is directly writing the data in the .c file of UDF and apply them onto inlet boundary.

Here is the program for the first situation.

/*you should execute the "openfile" before your calculation and execute closefile*/

/* after your computation to free your data file */

```
#include "udf.h"
static int last_ts = -1;
static float velocity;
FILE *fp;

DEFINE_PROFILE(velocity_profile, t, i)
{
   face_t f;
   int curr_ts;

/* read a data per timestep, you can read the data at any time          */
/* you like if you change the code below a little                       */
   curr_ts = N_TIME;

   if (last_ts != curr_ts)
   {
      last_ts = curr_ts;
      fscanf(fp,"%f\n",&velocity);
   }
   begin_f_loop(f, t)
       {
```

```
            F_PROFILE(f, t, i) = velocity;
        }
    end_f_loop(f, t)
}

DEFINE_ON_DEMAND(openfile)
{
    fp = fopen("c:\\data.txt", "rt");
    if(fp == NULL) Message("Data file can not be opened!\n");
    Message("Data file has been opened!\n");
}

DEFINE_ON_DEMAND(closefile)
{
    fclose(fp);
    Message("Data file has been closed!\n");
}
```

4.5.3 Operating Conditions

1. Operating pressure: Operating pressure is significant for incompressible ideal gas flows because it directly determines the density of the gas. The incompressible ideal gas law computes density as:

$$\rho = \frac{p}{\frac{R}{M_w}T} \qquad (4.14)$$

where M_w is Mach number. In this modeling, the operating pressure is assumed to be 1.013 bars. If the task involved is profile tracking then, the operating pressure is kept as default.

2. Operating density: The operating density is specified as 1.225 kg/m^3 in the modeling, as the experiment is carried out in atmosphere and that density is also taken into consideration. There the actual density in the momentum equation is computed by $(\rho - \rho_0)g$, since the fluid is in motion, by considering the Boussinesq model which results in faster convergence than you can get by setting up the problem with fluid density as a function of temperature(as here is not included). This model treats density as a constant value in all solved equations, except for the buoyancy term in the momentum equation:

$$(\rho - \rho_0)g \approx -\rho_0\beta(T - T_0)g \qquad (4.15)$$

where ρ_0 is the (constant) density of the flow, T_0 is the operating temperature, and β is the thermal expansion co-efficient.

3. Gravity: the gravity acceleration is given as 9.81m/s^2 along the positive x-direction.

4. Phased used: The phases used in the experiment is defined by their governing properties:

Air:

Density: 1.225 (kg/m^3)

Viscosity: 1.789e-4 (kg/m-s)

Material properties:

It is not able to list all the material properties parameters used in the simulation. Here just list the ones used in the experiments.

Table 4.2 Material parameters used in experiments

	Density	Viscosity	Surface Tension
De-ionized water	1000 kg/m^3	1.12 mPa·s	73.4e-3 N/m
PEDOT	1000 kg/m^3	9~20 mPa·s	51.5e-3 N/m

Table 4.3 Dispenser parameters used in printing

Glass capillary tube		PZT tube	
Inner radius	300um	Inner radius	375um
Outer radius	375um	Outer radius	675 um
Length	25.27mm	Length	15.99mm
Young's modulus	46Gpa		
Poisson's ratio	0.245		

4.5.4 Basic Simulating and Modeling Steps

The procedure in FLUENT for setting up a VOF model is outlined below:

1. Enabling the VOF model, specifying the number of phases (2 in the

experiment concerned), selecting the appropriate VOF formulation to be used (use time-dependent with the geometric reconstruction interpolation scheme) and turning on the Implicit Body Force treatment for the Body Force Formulation.

2. Coping with the material representing each phase from the materials database. If the material we want to use is not available in the database, new material can be created (here the new material is got by giving the corresponding material properties i.e. viscosity and density)
3. Defining the phases and specifying the interaction between them (e.g., surface tension). Here specify air as the primary phase and liquid material as the second phase because it is convenient to patch an initial volume fraction of 1 for it.
4. Since a body force (i.e., acceleration gravity) is used, the implicit body force options have to be turned on and also the gravity option specifying the value(here since x-axis is used, therefore along x-direction g=9.81 is entered)
5. Specifying the boundary conditions, including the secondary-phase volume fractions at flow boundaries (initial volume fraction =1, because it is assumed that the nozzle's capillary is filled with fluid).
6. Setting other model-specific solution parameters (user defined program for the axial velocity history at the nozzle).
7. Initializing the solution

8. Calculate a solution by iterating the problem and examine the result.

Chapter 5 Experiment System

This chapter provides a brief introduction of the system hardware. The DOD Inkjet printing system used in this study is made up of an XYZ-motion stage, a single print-head, temperature control, pneumatic control, a high-speed camera and a computer with a user interface to coordinate its motion and dispensing. The integrated 3D Inkjet Printing System is shown in Figure 5.1. The print-head is mounted on a XYZ stage with a resolution in the order of 1μm. The linear encoder is installed on the fast scanning X-axis for triggering the print-head as required.

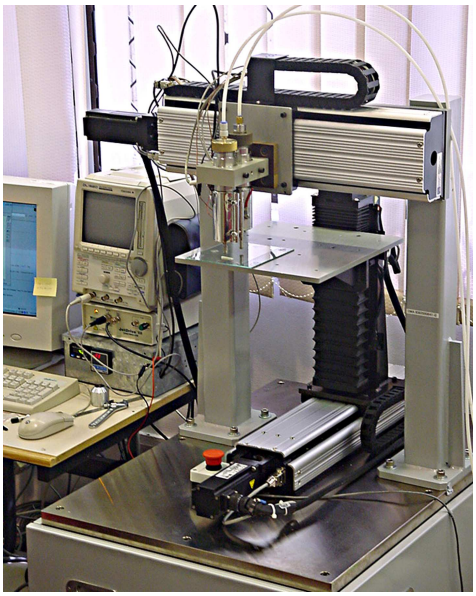

Figure 5.1: The integrated 3D Inkjet printing system integration

5.1 XYZ Stage Robot

The basic system of XYZ robot (see Figure 5.1) consists of each ball screw actuator driven by DC servo motor. The X-axis has a 1 μm/pulse resolution of linear encoder

with each output pulse, the Y-axis has a 1.25 μm/pulse resolution of rotary encoder built in the motor and the belt driven Z-axis has a 0.617 μm/pulse resolution.

The motion controller is a servo system, which is a complete closed-loop system that includes power amplifier, motor and encoder. The above robot is designed and built by DTI (Design Technology Institute), which is a stand-alone robot. The machine is equipped with a Galil motion controller (3 axis control) having external I/O that allows synchronous operations. There is a dedicated output port specifically for the output command function implemented for precise positioning.

5.2 Vacuum and Pressure Regulator

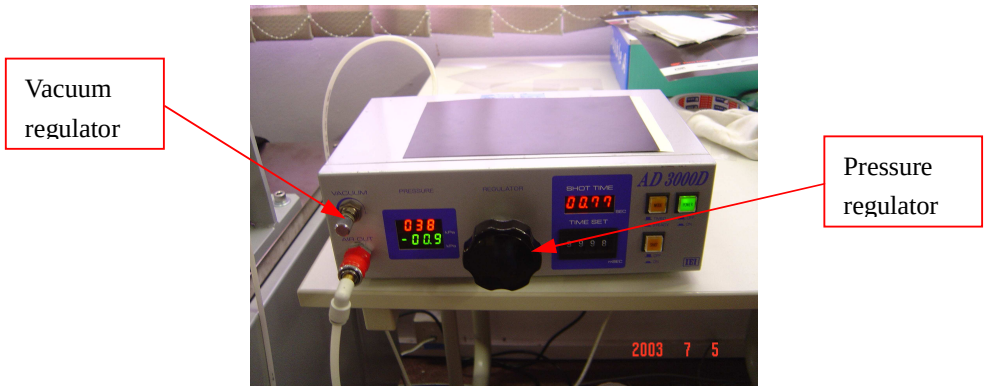

Figure 5.2: Vacuum and Pressure control unit / Compressor

The vacuum and pressure regulator unit (see Figure 5.2) is a requirement for the dispenser, which provides a set of vacuum (back pressure) pressure to minimize formation of meniscus on the dispenser nozzle (see Figure 5.3a). The pneumatic

device consists of a compressor, pressure controller and pneumatic tubes. The vacuum equipment allows the adjustment of the internal pressure in both positive and negative direction, to provide a consistent and stable fluid dispensing. Besides that, it also functions as generating purge to clear out the clogging in the glass tube.

The meniscus can cause the jetting to divert its path instead of being perpendicular to the nozzle surface (see Figure 5.3b) and therefore accuracy of drops is affected and even satellite forms during jetting. The vacuum has to be regulated depending on the pulse shape voltage set. Pressure regulator in this unit also provides a purge pressure to discharge the dispenser and reservoir as well as to clear any choke in the dispenser.

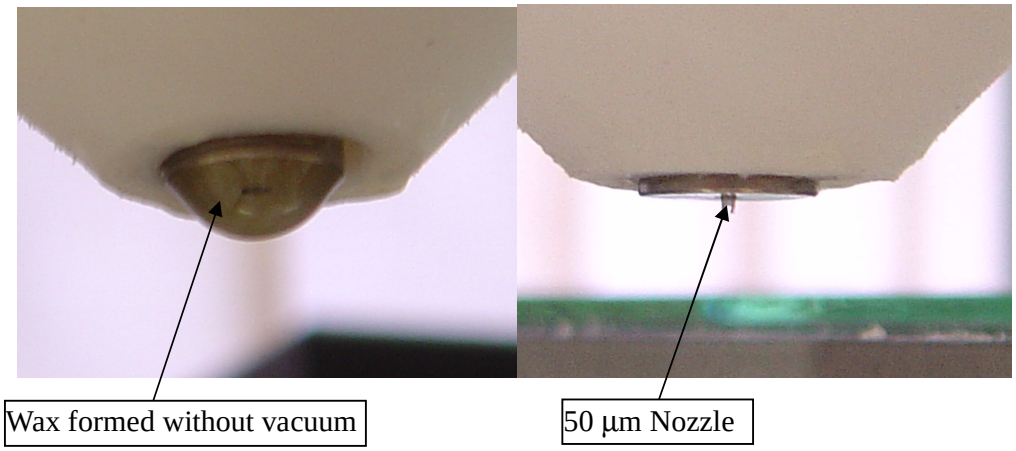

Figure 5.3: Meniscus formation on nozzle

5.3 Temperature Controller and Heater

There is also the standard industrial heater with a thermocouple and temperature controller, to obtain and maintain certain desired temperature. The control of the

temperature is limited to less than 240 ºC due to the operating temperature limit of dispenser.

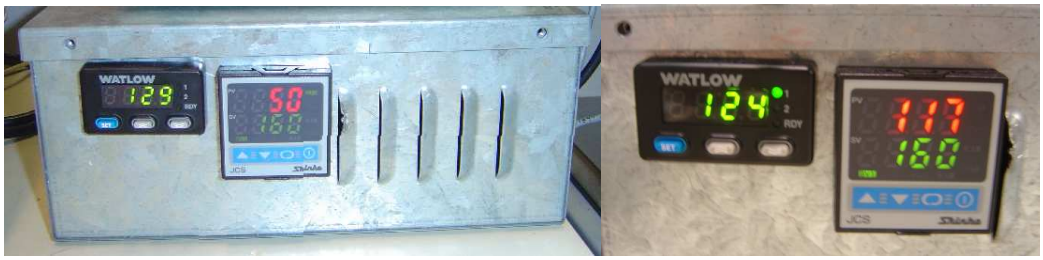

Figure 5.4: Temperature Controller

The above Figure shows the temperature controller and internally mounted with solid state relay to drive the heater ON/OFF. The dispenser able to take up to 200^{o}C of material fluid is good enough for molten solder. Coupled with the heater is a type-J thermocouple (see Figure 5.5) which provides a feedback and control to a desired temperature.

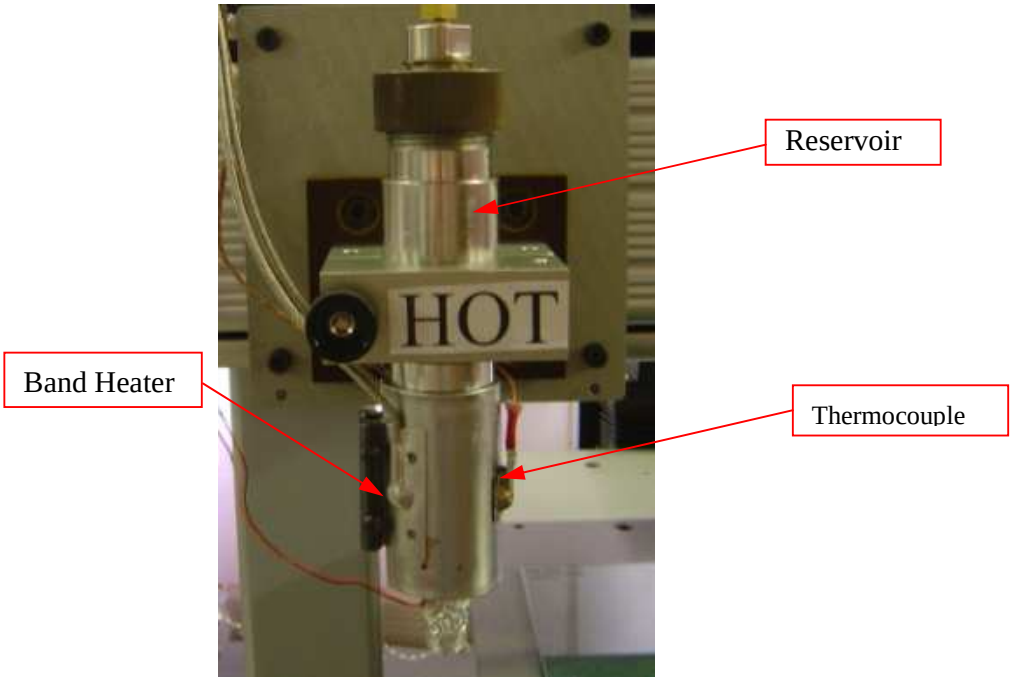

Figure 5.5: Heater and Thermocouple

5.4 Dispenser Unit

The print-head is the most vital part in this system. It generates the jetting of the droplets and controls the droplet size through the electrical waveform. The printhead consists of a dispenser (jetting device), reservoir cartridge, and filter. In this study, the inkjet print head from Microfab is adopted due to the features, such as broad working temperature range, high chemical resistance, etc, as shown in Figure 5.6. The glass tube has an orifice at the exit which ranges with size from 25μm to 100 μm. The size of the orifice can be selected depending on the droplet size and viscosity of the material.

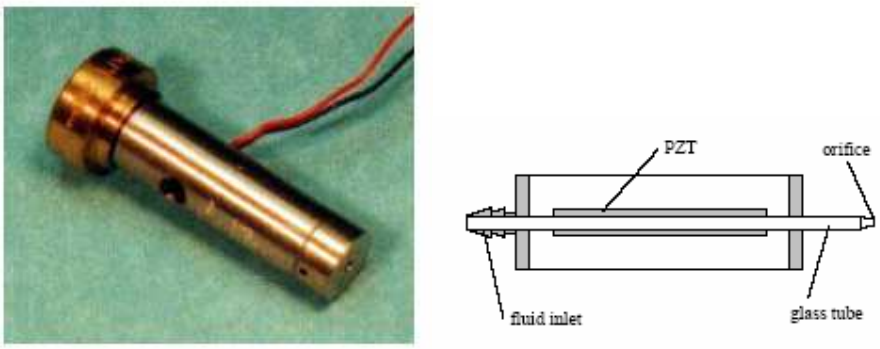

Figure 5.6 Dispenser and schematic diagram

The piezo actuator mounted around of the tube provides a squeeze effect when there is voltage applied at certain frequency usually at maximum 20 kHz. The print head used for the experiments is the high-temperature Solder Jet® 50µm nozzle from MicroFa, with. PZT-5H piezo-actuated tube. The elastic modulus of the capillary glass tube is 46Gpa and Poisson's ratio is 0.245.

Some physical parameters are given as follow for the purpose of computation study. The constitutive data of PZT-5H is presented in the Strain-Charge format.[72]

Compliance:

$$S_E = \begin{bmatrix} 16.5 & -4.78 & -8.45 & 0 & 0 & 0 \\ -4.78 & 16.5 & -8.45 & 0 & 0 & 0 \\ -8.45 & -8.45 & 20.7 & 0 & 0 & 0 \\ 0 & 0 & 0 & 43.5 & 0 & 0 \\ 0 & 0 & 0 & 0 & 43.5 & 0 \\ 0 & 0 & 0 & 0 & 0 & 42.6 \end{bmatrix} * 10^{-12} \frac{m^2}{N}$$

Piezoelectric Coupling:

$$d = \begin{bmatrix} 0 & 0 & 0 & 0 & 741 & 0 \\ 0 & 0 & 0 & 741 & 0 & 0 \\ -274 & -274 & 593 & 0 & 0 & 0 \end{bmatrix} * 10^{-12} \frac{C}{N}$$

Relative Permittivity:

$$\frac{\varepsilon_T}{\varepsilon_0} = \begin{bmatrix} 3130 & 0 & 0 \\ 0 & 3130 & 0 \\ 0 & 0 & 3400 \end{bmatrix}, \varepsilon_0 = 8.854 * 10^{-12} \frac{F}{m}$$

5.5 Dispenser Controller

The controller (see Figure 5.7) provides a pulse generator to drive the piezo actuator. A separate unit to drives a strobe LED for observing droplets in flight that works from the strobe TTL output of the controller. A high speed camera is used to capture drop images as it starts to jet out from the nozzle to the substrates surface. The table below shows the controller technical information with regard the pulse shape simulation, maximum frequency, etc. It is mostly operating in single-pulse mode, whereby the motion controller externally triggers the master trigger port of the dispenser controller.

Figure 5.7 Dispenser controller units

Table 5.1 Controller physical information

DC voltage UI	-140 to 0 V
Voltage level 1	UI to +140 V
Voltage level 2	-140 V to UI
Rise time (DC to level 1)	1 - 3276 µs total pulse length < 4095 µs
Level 1 time	3 - 3276 µs total pulse length < 4095 µs
Fall time (level 1 to level 2)	1 - 3276 µs total pulse length < 4095 µs
Level 2 time	3 - 3276 µs total pulse length < 4095 µs
Final rise time (level 2 to DC)	1 - 3276 µs total pulse length < 4095 µs
Frequency	1 Hz - 20 kHz
Pulse modes	single, burst, continuous
Burst count	1 - 999
Control	(1) RS-232-C (2) external TTL trigger (2.5-5 V >0.5 µs rising flank sets timing)
Strobe output	1 TTL per 1-64 triggers -500 µs to +2500 µs relative to trigger programmable and manual adjustments
Connectors	RS-232-C, 9 pin female; HV, DIN; external trigger and strobe out-put, BNC
Power supply	110 V or 220 V internally set

Size	9 ¾" × 7 ½" × 2 ¾" / 25 cm × 19 cm × 7 cm

5.6 Camera System

Drop ejection process is observed by a JAI CV-A11 camera from Ultravision Pte Ltd., which is rigidly mounted such that it focuses on the area directly about the samples. With the appropriate zoom settings, the accumulation of the droplets can be observed and measured. Additional benefit of the camera system is that any misalignment along X and Y directions would not occur because the measurement is done once the printing is completed without shifting the sample.

When a signal is sent to the printhead, a trigger signal can be also sent to the stroboscope. Stroboscope is widely used to freeze the motion of high-speed objects. When the driver is set in continuous mode and providing that the dispensing process is stable and repeatable, the drop formation and motion can be clearly seen under either of the two trigger mode: external or internal mode.

Under external mode, the frequency of the stroboscope is set to be the same as that of the piezo tube. By adjusting the time delay of the between these two signals (signal for the stroboscope and signal for the piezo tube), the whole drop ejection process can be seen clearly by a series of stationary frame in time sequencing, as shown in the Figure 5.8. Under internal mode, stroboscope frequency is set to be slightly lower than the frequency for the piezo tube. By decreasing the difference between such two

frequencies, the “observed” speed of the droplet ejection is also decreasing.

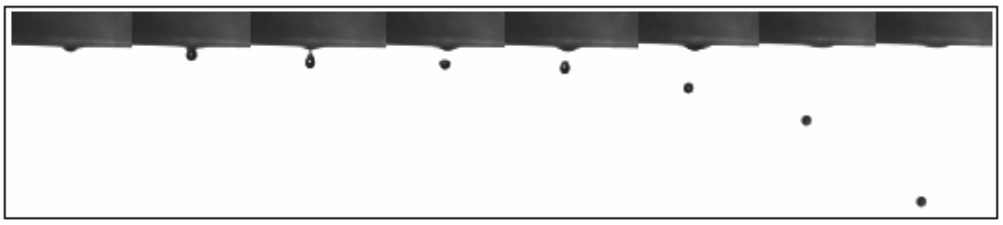

Figure 5.8 A series of stationary frame caught at 200, 265, 360, 410, 520, 900, 1200 and 2500 μs.

Chapter 6 Results and Discussion

This chapter explains and discusses the numerical results obtained from the constructed model, and also gives a comparison of numerical and experimental results to verify the accuracy of the model. In the first section, it describes the three main stages during the drop ejection process and discusses the effect of the Reynolds number and Capillary number on the dynamics of drop formation. In the second section, the model, which uses de-ionized water and PEDOT as the fluid materials, is evaluated in terms of droplet velocity and drop volume.

6.1 Numerical Results and Discussion

6.1.1 Drop Ejection Process

Figure 6.1 shows during drop formation process, three cases of surface profiles generated with different material parameters used in Table 6.1. The reason using A, B and C material is because these three kinds of materials with different properties will produce three typically different surface profiles. As shown in Figure 6.1 (A) the ejected liquid finally forms a spherical shape without long tail and satellite. In (B) a satellite droplet is generated and lies between the primary drop and the cone-shaped liquid remaining pendant on the tube. In (C) a thin and long tail is formed and following the main drop after detaching from the nozzle. The droplet shape is determined by the competition among surface tension, inertial force and viscous force. In the following discussion, the influence of surface tension, inertial force and viscous

force on the dynamics of drop formation is represented by the Reynolds number and Capillary number. Figure 6.1, 6.2 and 6.3 are in the same scale with dimensions of 0.0255 mm X 0.004mm.

Table 6.1 Material parameters used in the simulation model

	Density (kg/m^3)	Viscosity (mPa·s)	Surface Tension (N/m)
A	1000	2	7.34e-3
B	846	6.19	28.999e-3
C	1000	1.12	73.4e-3

The drop ejection process is generally divided into three main stages.

(1) The first stage is the droplet formation process, where the liquid ejected from the nozzle gradually changes its shape from a meniscus to a cylindrical column, [58] [59] as shown in Figures 6.1 A(a)-(d), B(a)-(d), C(a)-(f). The droplet length increase at different conditions, but the shape of the droplet is almost same.

(2) The second stage is the droplet breaking process, [58] [59] and is shown in Figures 6.1 A(e)-(g), B(e)-(i), C(g)-(k).The droplet changes shape from a cylindrical column to a tear-like shape, because the ejected liquid has a higher velocity at the droplet tip than at the nozzle exit. The occurrence of neck probably results from the face that a back-drawing force is exerted inside the nozzle on the fluid with larger surface

tension.

(3) The third stage is the droplet flying process [58] [59] shown in Figures 6.1 A(h)-(m), B(j)-(m), C(l)-(m). At this stage, the liquid column is completely separated from the nozzle exit. The tail, whether it is long or short, moves towards the head in a short time and the droplet shape is finally almost a sphere.

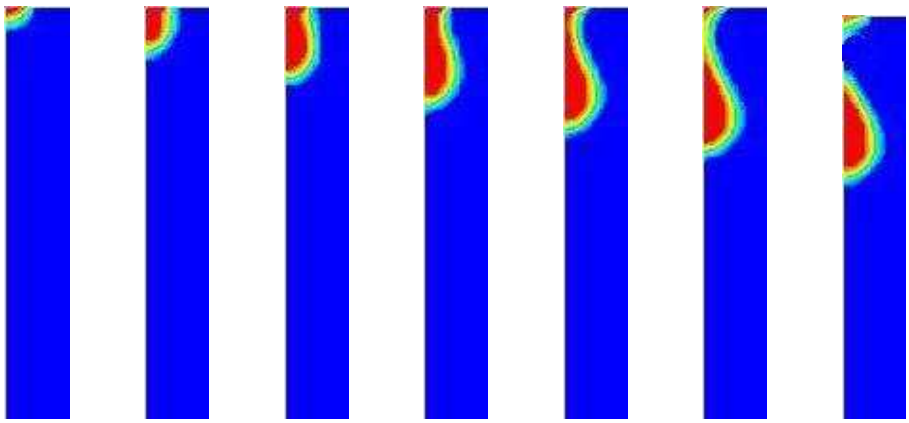

(a)t =10μs (b)t =20μs (c)t =30μs (d)t =40μs (e)t =50μs (f)t =60μs (g)t =70μs

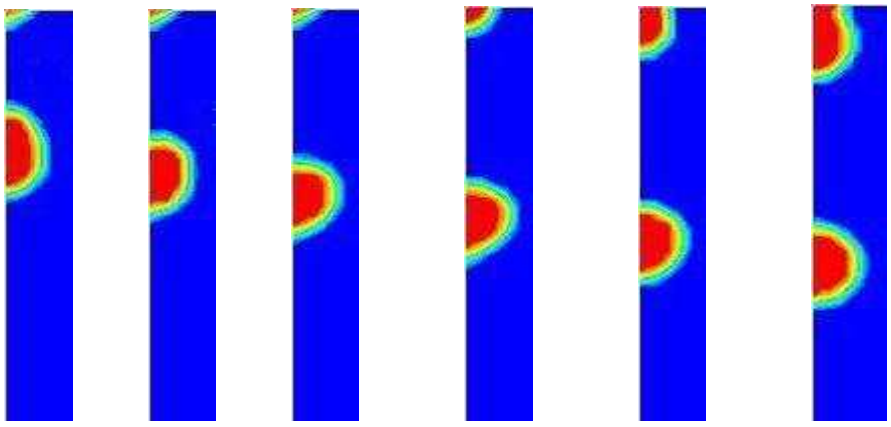

(h)t =80μs (i)t =90μs (j)t =100μs (k)t =110μs (l)t =120μs (m)t =130μs

(A)

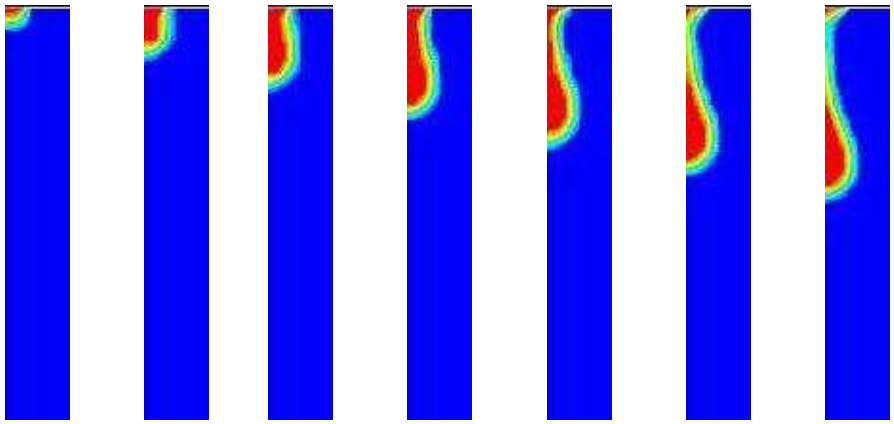

(a)t =10μs (b)t =20μs (c)t =30μs (d)t =40μs (e)t =50μs (f)t =60μs (g)t =70μs

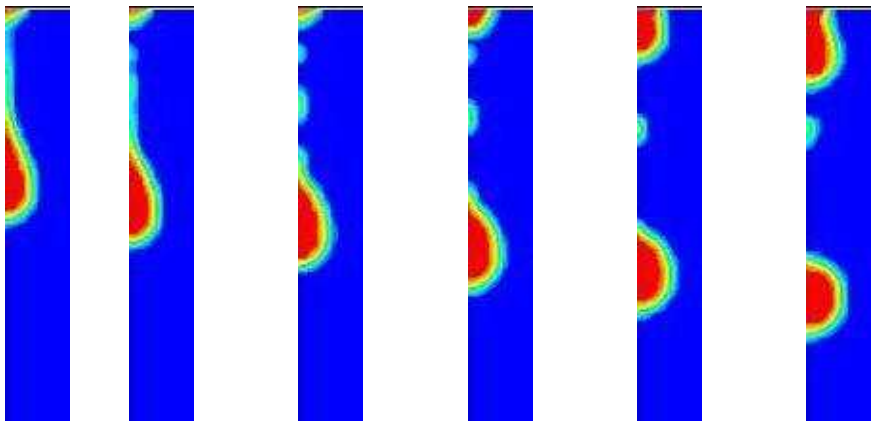

(h)t =80μs (i)t =90μs (j)t =100μs (k)t =110μs (l)t =120μs (m)t =130μs

(B)

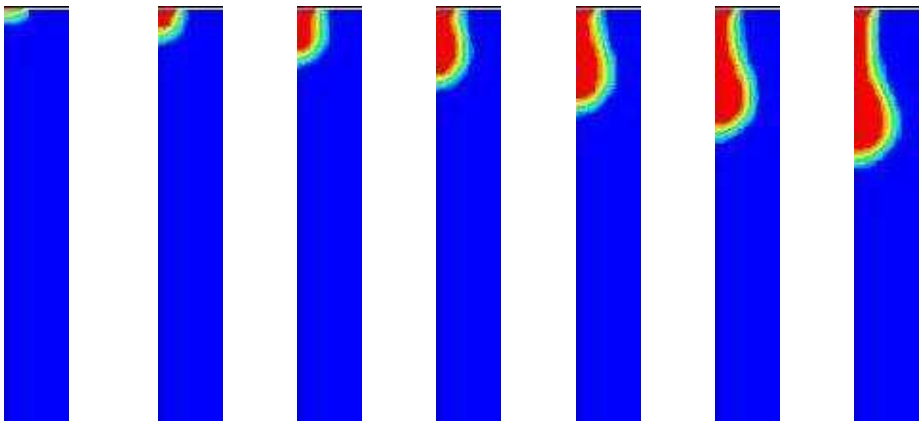

(a)t =10μs (b)t =20μs (c)t =30μs (d)t =40μs (e)t =50μs (f)t =60μs (g)t =70μs

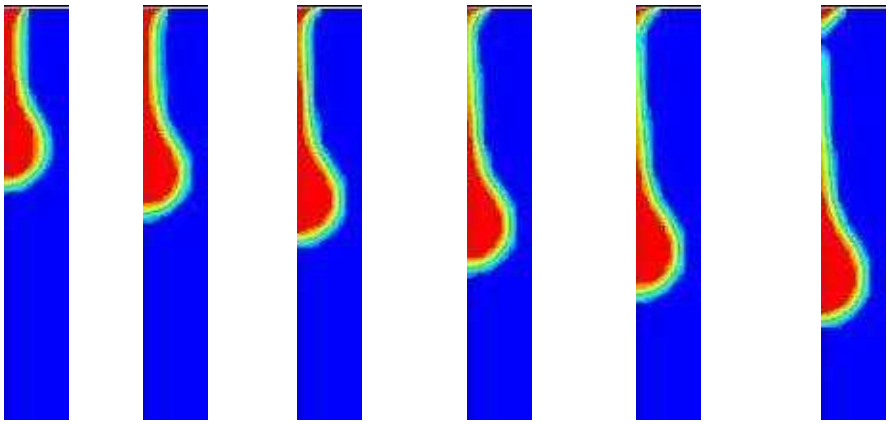

(h)t =80μs (i)t =90μs (j)t =100μs (k)t =110μs (l)t =120μs (m)t =130μs

(C)

Figure 6.1 Simulation results of drop formation process with different material parameters

6.1.2 Effect of Reynolds and Capillary Number

Reynolds number represents the ratio of inertial forces relative to viscous forces. It is defined as $\mathrm{Re} = \rho v_s L / \mu$, where v_s is mean fluid velocity, L is characteristic length, μ is fluid viscosity and ρ is fluid density. Capillary number represents the relative effect of viscous force versus surface tension. It is defined as $Ca = \mu v / \sigma$, where μ is the viscosity of the liquid, v is a characteristic velocity and σ is the surface or interfacial tension between the two fluid phases. Calculations are performed by varying one parameter while keeping the others fixed. The Reynolds number, Re, is varied in the range of 0.1 to 100.0. The capillary number, Ca, is varied in the range of 0.1 to 1.0.

Effect of Reynolds Number

The effect of the Reynolds number on drop breakup, in terms of the dimensionless

limiting length, L/R, is shown in Figure 6.2. It shows four surface shapes of drop at the instant they are about to break off from the nozzle with Re=0.1, 1.0, 10.0, 100.0 and a constant capillary number Ca=0.01. The limiting length is 3.75, 3.70, 5.2, 5.53 in (a)-(d) of Figure 6.2, respectively. It increases monotonically as the Reynolds number increase, due primarily to the increase in the inertial force to elongate the liquid pendant on the nozzle. Moreover, it also indicates that along with the increasing elongation of the liquid pendant on the nozzle at the large Reynolds number, the tip of the liquid pendant rebounds at a high velocity and forms a bulbous due to unbalanced capillary force. No satellite droplet is generated at large Reynolds number.

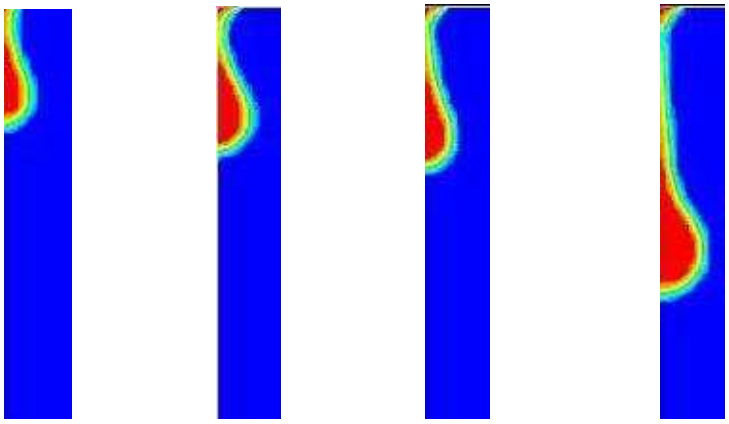

(a) Re=0.1 (b) Re=1.0 (c) Re=10.0 (d) Re=100.0

Figure 6.2 Drop breakups at different Reynolds numbers

Effect of Capillary Number

Figure 6.3 demonstrates four drop profiles at the instant of breakup at a constant Reynolds number of Re=1. The dimensionless limiting length, L/R, is 3.94, 4.24, 5.63 and 5.98 at Ca=0.1, 0.2, 0.5 and 1, respectively. It is obvious that the limiting length

increase monotonically as Ca increases. The different capillary numbers can be changed easily by varying the surface tension or viscosity. As shown in Figure 6.3, the decrease in surface tension leads to the reduction of the force holding the drop on the tube and results in the significant delay of drop breakup. High viscous liquids also produce a relatively longer breakup time with relatively slower droplet flight velocity because of the intensely viscous dissipation. Therefore, the liquid remaining the tube accumulates and causes a larger and longer liquid cone pendant at the nozzle prior to detachment of the primary drop.

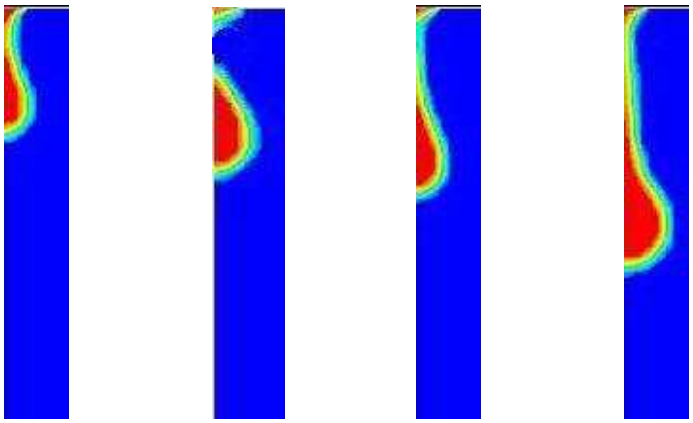

(a) Ca=0.1 (b) Ca=0.2 (c) Ca=0.5 (d) Ca=1.0

Figure 6.3 Drop breakups at different capillary numbers

6.2 Comparison of Results

This section provides comparison between the simulation and experiment results of the drop formation to evaluate the numerical simulation model. The evaluating items are droplet velocity, drop volume and shape. The fluid materials used are de-ionized water and PEDOT.

6.2.1 Calculation of Droplet velocity, $V_{droplet}$

The drop velocity is calculated using the formula for velocity,

$$V_{speed} = \frac{L}{T}$$

where L is distance traveled by the droplet and T is time taken for dispensing through L.

6.2.2 Droplet Volume Measurement

Due to the limits in the measuring equipment used, the following method was used to calculate volume of each dispensed droplet.

The droplet is first assumed to be spherical in shape. The diameter (D) of the droplet is measured using the same scale as in the calculation of velocity. Through applying the formula for volume of sphere,

$$V_{droplet} = \frac{4\pi\left(\frac{D}{2}\right)^3}{3}$$

The volume of each dispensed droplet can be calculated.

6.2.3 PEDOT

PEDOT is an aqueous conductive polymer ink belongs to the intrinsically conductive polymer (ICP) group of polymer inks. It is widely used as a hole-transport layer to improve the performance of OLED. Its density, dynamic viscosity, surface tension, are 1.0 g/cm^3, 9~20e-3 N·s/m^2, 0.0515 N/m, respectively. For a uni-polar pulse wave, the

optimized printing parameters are listed in the Table 6.2. The frequency is fixed at 100 Hz, and the back pressure is at - 1.2 kPa. The simulation results are also generated by using these parameters.

Table 6.2 Control parameters used in PEDOT printing

Uni-Polar Pulse Wave Parameters	Settings
Rise time	3 μs
Dwell Time	35μs
Fall time	3 μs
Voltage	40V

Other Parameters	Settings
Frequency	100 Hz
Back Pressure	- 1.2 kPa

The drop shapes from the simulated images are similar to those from the experimental ones. In the drop formation stage (Figure 6.4, a-d), the ejected liquid from the nozzle changes gradually from meniscus to cylindrical column in the both pictures and the drop shapes look much the same with each other. In the droplet breaking process (e-h), the tear-like shape with neck occurs at the same time, but the size of the liquid pendant on the nozzle in the experiment is a little bigger than that in the simulation. In the drop flying process (i-k), the round droplets fly followed by the satellites in both experimental and simulated images. The difference is that there are two satellites in simulation result and one in experimental result. The reason is probably the double breakage of the liquid neck in simulation. The neck breaks at its lower end by the

weight of a detaching drop. The unbalanced capillary forces exist on the neck after its first breakup, the neck recoils. The occurrence of the secondary breakup at its upper end leads to the generation of the second satellite droplets. Finally, the second satellite is joined by the ejected liquid from the nozzle. It is possible that the force generated inside the tube push the ejected liquid faster than second satellite.

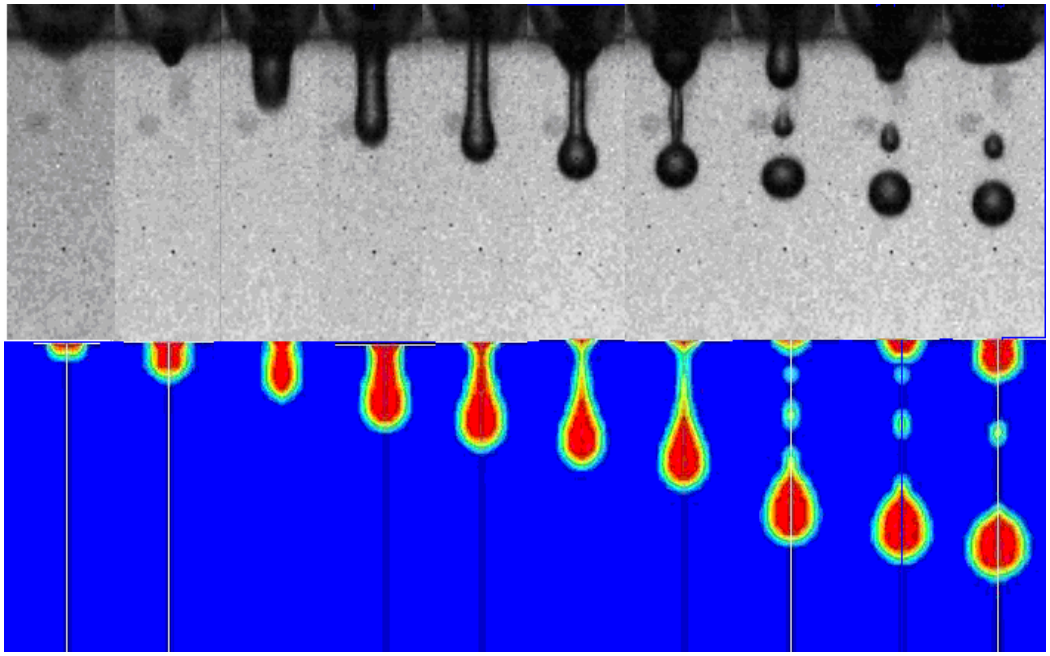

(a) (b) (c) (d) (e) (f) (h) (i) (j) (k)

Figure 6.4 Comparison of pictures and simulation results of drop generation of PEDOT (Left-right: 10μs, 20μs, 30μs, 40μs, 50μs 60μs, 70μs, 80μs, 90μs, 100μs)

The diameter of the drop measured from simulation is 62.50μm compared with the experimental one with 61.90μm. Using the formulation of drop volume, the result of simulation is $1.278*10^{-13}$ m^3 and the one of the experiment is $1.241*10^{-13}$ m^3. The velocity of the drop determined from simulation is about 2.09 m/s which agree with

the experimental one at about 2.42 m/s. The percentage errors of drop volume and drop velocity are 2.9% and 13.6%, respectively. All the percentage errors are in the error range of 20%.

Table 6.3 Comparison of experimental and simulation results

	Experimental Value	Simulation Value	Percentage Error
Drop Volume	$1.241*10^{-13}\ m^3$	$1.278*10^{-13}\ m^3$	2.9%
Drop Velocity	2.42 m/s	2.09 m/s	13.6%

6.2.4 De-ionized Water

De-ionized water is chosen for the fluid in the print head. Its density, dynamic viscosity, surface tension, speed of sound are 1.0 g/cm^3 ,1.12e-3 $N{\cdot}s/m^2$, 7.34e-2 N/m and 1435m/s, respectively. For a uni-polar pulse wave, the optimized printing parameters are listed in the Table 6.4. The frequency is fixed at 100 Hz, and the back pressure is at - 1.0 kPa. These parameters are also applied in the simulation model.

Table 6.4 Control parameters used in de-ionized water printing

Uni-Polar Pulse Wave Parameters	Settings
Rise time	3 μs
Dwell Time	38μs
Fall time	3 μs
Voltage	45V

Other Parameters	Settings
Frequency	100 Hz
Back Pressure	- 1.0 kPa

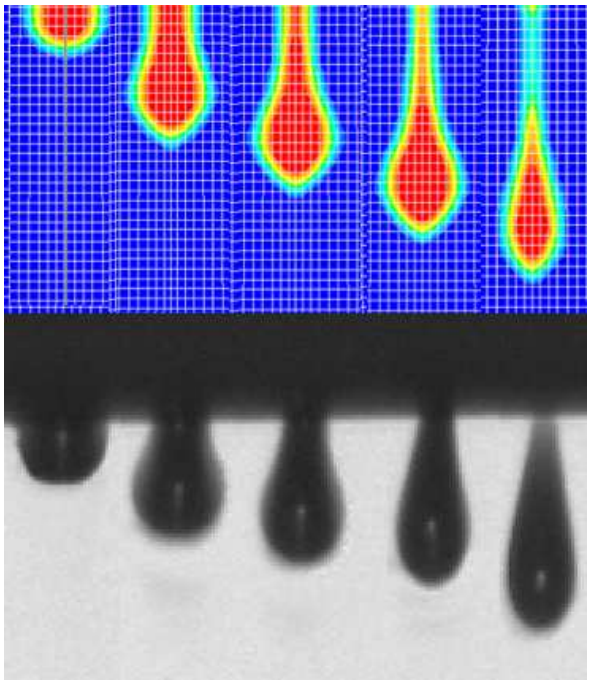

Figure 6.5 Comparison of pictures and simulation results of drop generation of water

(Left-right: 20μs, 40μs, 60μs, 80μs, 100μs)

Figure 6.5 shows the comparison of the simulation and experiment results of droplet of de-ionized water. In the time period of 0-40μs, the meniscus occurs at the nozzle exit in both simulation and experiment. In the following time of 40-80μs, the liquid ejected from the nozzle gradually changes its shape from a meniscus to a cylindrical column, and to a tear-like shape in the both experimental and simulated images. In the time period of 80-100μs, necks become longer and longer and the droplet shape is finally almost a sphere. The simulated neck is thinner than that of experiment. The numerically obtained results have slightly pointed effect over the experimental one. The underestimation of the inertial force is likely to have given rise to the difference

between calculated and observed results.

Table 6.5 Comparison of experimental and simulation results

	Experimental Value	Simulation Value	Percentage Error
Drop Volume	$1.13*10^{-13}\ m^3$	$1.15*10^{-13}\ m^3$	1.6%
Drop Velocity	2.04 m/s	2.35 m/s	15%

Table 6.6 Velocities of drop with different no. of Fourier series terms

No. of Fourier Series Terms		20	30	40	50
PEDOT	Velocity (m/s)	1.97	2.02	2.09	2.67
	Error Percentage	18.8%	16.4%	13.6%	14.5%
Water	Velocity (m/s)	2.45	2.42	2.35	2.36
	Error Percentage	20.3%	18.5%	15%	16.1%

Figure 6.5 shows the comparison of the simulation obtained from two-dimensional axisymmetric CFD-VOF with the experimental results like the pictures taken from a camera with million frames per second. The external profile of the simulated droplet is similar to that of the experimental pictures taken in the time period of 20-80μs, but at 100μs the simulation droplet has a longer tail of 235.28μm than experimental one of 204μm. The diameter of the drop measured from simulation is 60.32μm compared with the experimental one with 60μm. A look at the velocity of the drop determined from simulation is about 2.35 m/s which agree with the experimental one at about 2.04 m/s. The percentage errors of drop volume and drop velocity are 1.6% and 15%,

respectively. All of percentage errors are less than 20% as well.

6.3 Discussion

The computational time required for PEDOT and de-ionized water are 1838s and 1794s, respectively, compared to 4625s for Ethylene glycol in Shin's research [67]. In this study, the large portion of the whole computational time is taken to calculate the axial velocity at the nozzle and the number of the Fourier series terms is one of the factors affecting the computational time. For instance, the time, which is taken just for the calculation of the axial velocity at the nozzle, are 1374s, 1515s, 1737s and 2019s with 20, 30, 40 and 50 Fourier series terms, respectively. According to the simulated results of drop velocities with different number of Fourier series terms in Table 6.6, it is found that the simulated drop velocities with 40 Fourier series terms have the percentage error of 13.6% for PEDOT, and 15% for de-ionized water, which both are less than the other cases.

The percentage error of the drop velocity is 13.6% for PEDOT, and 15% for de-ionized water, compared to 47.70% and 47.52% for different cases in Shin's simulation work [67]. The percentage error of drop volume is 2.9% for PEDOT, and 1.6% for de-ionized water. The potential reason for the difference in simulation and experiment may result from the linearized Navier-Stokes z momentum equation which ignores the convective acceleration terms. Another source of the difference may be from the occurrence of mass loss at the nozzle tip. As the fluid is ejected from the

nozzle, the mass loss would happen by fluid returning from the fluid jetted outside the nozzle, which has been spotted in Shin's simulated results. [67] The third possible source is capillary force combined with the viscous effect in the fluid giving rise to momentum redistribution in the fluid outside the nozzle, which results in less forward momentum of the ejected drop than the net momentum. It is noted that the error percentage for drop velocity is larger than the one for drop volume, probably resulting from calculation based on length of drop thread over time. The break of thread and its length is driven by the capillary force. This causes the large difference between velocity and volume calculation due to the lack of consideration of capillary force in the simulation.

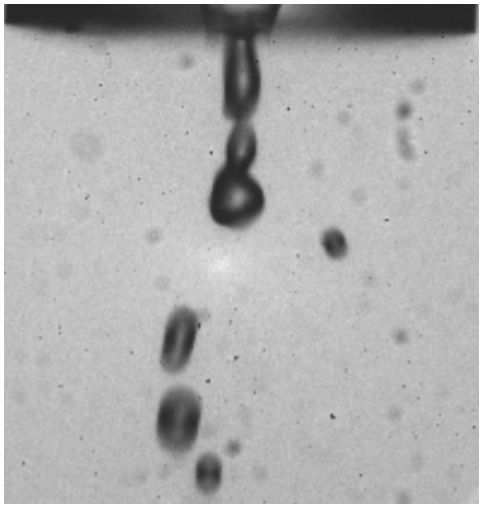

Figure 6.6 Ejection of the water with satellites

The difficult problem in the experiment is to obtain stable drop formation images. The extremely small diameter and volume of the single droplet is easily affected by the ambient environment, which results in the oblique flying of the droplet. The small

nozzle of the dispenser is probably clogged by the high viscous liquid. Sometimes the profile of the forming droplet is not a tear-like shape desired, which possibly resulting from the effect of surface tension (Figure 6.6).

Attempts to solve these problems include: performing the experiment with a shield to prevent the air from blowing the droplet; using liquid with as less viscosity as possible; regulating the controlling parameters like voltage, dwell time or back pressure, when the surface tension is not enough to hold the droplet.

Another issue encountered is to calculate the volume of the droplet when its image is blurred. Firstly, it is required to outline a clear edge of the drop in the image, including the blurred portion of the droplet, as this unclear part also contains the volume of the fluid ejected from print head. Secondly, there is the issue of finding the expected circular diameter of droplet outline. Most of the droplets are not spherical in shape; so the expected circle is used as the substitution of the actual droplet shape for calculation purpose. This method is applied in the simulation computation as well.

Chapter 7 Conclusions and Recommendation

7.1 Conclusions

The main objective of numerical simulation of the dynamics of drop formation ejected from the nozzle of micro-dispenser is to get the ejection characteristics of droplet, such as its size, volume, velocity and drop evolution, without experiment for improving the quality of inkjet printing and understanding the fact of drop formation better.

In this thesis, an analytical method is used to analyze the oscillatory fluid movement inside a squeezed-type piezoelectric cylindrical inkjet print head with tapered nozzle. Comparing with the earlier researcher, the printhead is divided into four parts: unactuated part1 (without connecting with the nozzle part), actuated part1, unactuated part 2 (connected with the actuated part and the nozzle part) and nozzle part. The pressure and velocity functions for each part are derived and these functions with unknown coefficients are solved together with the experimentally obtained upstream pressure boundary condition of a back pressure, neither applying zero pressure nor regarding the capillary glass tube as semi-infinite tube. The axial velocity history at the nozzle exit is obtained in the form of an oscillatory function in time domain. It is recommended that 40 Fourier terms be used for the computation and simulation, since it shows the advantage of compromise of time-saving and good simulation results.

The two dimensional axisymmetric numerical simulation model of the drop formation from the nozzle has been developed with Volume-of-Fluid (VOF) method. The VOF method tracks the interface profile between two immiscible phases, coupled with the Piecewise-Linear Interface Calculation (PLIC) techniques in each cell. Surface tension is implemented by the Continuous Surface Force (CFS) method.

The process of drop ejection is divided into three stages: droplet formation process, droplet breaking process, and droplet flying process. The droplet shape is determined by the competition among surface tension, inertial force and viscous force. In the following discussion, the influence of surface tension, inertial force and viscous force on the dynamics of drop formation is represented by the Reynolds number and Capillary number. The limiting length increases monotonically as the Reynolds number increases, due primarily to the increase in the inertial force to elongate the liquid pendant on the nozzle. The limiting length also increases monotonically as Capillary number increases due to the reduction in surface tension leading to the decrease of the force holding the drop on the tube and results in the significant delay of drop breakup.

This simulation model is able to predict the ejected droplet size or volume, and velocity and the model is dependent on the type of the tube and the geometry. By comparing the simulation and experiment results of PEDOT droplet, the drop volume

is $1.278*10^{-13}\,m^3$ and $1.241*10^{-13}\,m^3$, and the velocity of the drop is about 2.09 m/s and 2.42 m/s. The percentage errors of drop volume and drop velocity are 2.9% and 13.6%, respectively. In the case of de-ionized water, the drop volume is $1.15*10^{-13}\,m^3$ and $1.13*10^{-13}\,m^3$ obtained from simulation and experiment. The velocity of the drop determined from simulation is about 2.35 m/s which agree with the experimental one at about 2.04 m/s. The percentage errors of drop volume and drop velocity are 1.6% and 15%, respectively. All the percentage errors are in the error range of 20%.

7.2 Future Research Work

- In this simulation model, the fluid material is estimated as Newtonian fluid for simplicity. But in inkjet printing manufacturing, most of materials used are polymer solution, some with small particles. The simulation of ejection of the fluid with particle can be considered. In FLUENT, a function can be used to represent the viscosity instead of a constant in this model.
- The impact of the droplet on the substrate is closely related to the accuracy and quality of the inkjet printing. This model just simulates the drop ejection process. The simulation of the impacting process of drop on the substrate can be continued.
- Use the developed model to generate a group of controlling data for certain diameter of droplets, and then the operator use these data to set the optimal time, applied voltage, frequency and back pressure.
- This simulation model analyses the squeezed-type piezo inkjet printhead from

Micofab. If the structure of the printhead is changed, it is necessary to investigate the new structure of the dispenser and the fluid motion inside the dispenser to renew the axial velocity at the orifice for the purpose of precise simulation.

References

[1] http://en.wikipedia.org/wiki/Inkjet_printing

[2] Osman A. Basaran, Small-scale free surface flows with breakup: drop formation and emerging applications. AIChE Journal Vol. 48, No.9, 1842-1848 (2002).

[3] Berend-Jan de Gans, Paul C. Duineveld and Ulrich S. Schubert, Inkjet Printing of Polymers: State of the Art and Future Development. Adv. Mater.16, No.3, 203-213 (2004).

[4] Jurgen Brunahl and Alex M. Grishin, Piezoelectric shear mode drop-on-demand inkjet actuator, Sensors and Actuators A 101, 371-382 (2002).

[5] Clift, R., Grace, J. R., and Weber, M. E., Bubbles, Drops, and Particles. Academic Press, New York, (1978).

[6] Peregrine, D.H., Shoker, G., & Symon, A. The bifurcation of liquid bridge. Journal of Fluid Mechanics 212, 25-39 (1990).

[7] P. K. Notz, A. U. Chen, and O. A. Basaran, Satellite drops: Unexpected dynamics and change of scaling during pinch-off, Phys. Fluids 13, 549 (2001).

[8] D. M. Henderson, W. G. Pritchard, and L. B. Smolka, On the pinch-off of a pendant drop of viscous fluid, Phys. Fluids 9, 3188 (1997).

[9] T. A. Kowalewski, On the separation of droplets from a liquid jet, Fluid Dyn. Res. 17, 121 (1996).

[10] X. Zhang and O. A. Basaran, An experimental study of dynamics of drop formation, Phys. Fluids 7, 1184 (1995).

[11] Weathers, P. W., Internal Flow Patterns of Forming Liquid Drops. MS thesis, Iowa State Univ., (1971).

[12] Humphrey, J. A. C., Hummel, R. L., and Smith, J. W., Experimental study of the internal fluid dynamics of forming drops. Canadian Journal of Chemical Eng. V52, 449-456 (1974).

[13] Pilch, M., Erdman, C.A., Use of breakup time data and velocity history data to predict the maximum size of stable fragments for acceleration-induced breakup of a liquid drop. Int. J. Multiphase Flow 13, 741–757 (1987).

[14] Gelfand, B.E., Droplet breakup phenomena in flows with velocity lag. Prog. Energy Combust. Sci. 22, 201–265 (1996).

[15] Shi, X.D., Brenner, M.P., & Nagel, S.R. A cascade of structure in a drop falling from a faucet. Science, 265, 219-222 (1994).

[16]Huaxiong Huang, Non-Newtonian effects on ink-jet droplet formation, NAW 5/6 nr. 1 mart, 63-68 (2005).

[17] M. P. Brenner, J. Eggers, K. Joseph, S. R. Nagel and X. D. Shi, Breakdown of scaling in droplet fission at high Reynolds numbers, Phys. Fluids 9, 1573 (1997).

[18]Y. Christanti and L. M. Walker, Surface tension driven jet break up of strain-hardening polymer solutions, J. Non-Newtonian Fluid Mech. 100, 9 (2001).

[19] Y. Christanti and L. M. Walker, Effect of fluid relaxation time of dilute polymer solutions on jet breakup due to a forced disturbance, J. Rheol. 46, 733 (2002).

[20] R. P. Mun, B. W. Young, and D. V. Boger, Atomization of dilute polymer solutions in agricultural spray nozzles, J. Non-Newtonian Fluid Mech. 83, 163 (1999).

[21] R. P Mun, J. A. Byars, and D. V. Boger, The effects of polymer concentration and molecular weight on the breakup of laminar capillary jets, J. Non-Newtonian Fluid Mech. 74, 285 (1998).

[22] R. Crooks and D. V. Boger, Influence of fluid elasticity on drops impacting on dry surfaces, J. Rheol. 44, 973 (2000).

[23] F.R.S. Rayleigh, On the instability of jets, Proc. London Math. Soc. 10 (4) 4-13 (1878).

[24] Scheele, G.F., & Meister, B.J. Drop formation at low velocities in liquid-liquid systems: Part I. Prediction of drop volume. A.I.Ch.E. Journal 14, 9-19 (1968).

[25] Heertjes, M.P., de Nie, L.H., & de Vries, H.J. Drop formation in liquid-liquid systems - I Prediction of drop volumes at moderate speed of formation. Chemical Engineering Science 26, 441-449 (1971).

[26] Michael, D.H. Meniscus stability. Annual Review of Fluid Mechanics 13, 189-215 (1981).

[27] Keller, J. B., and M. J. Miksis, Surface Tension Driven Flows, SIAM J. Appl. Math., 43, 268 (1983).

[28] J. Eggers, Universal pinching of 3D axisymmetric free-surface flow, Phys. Rev. Lett. 71, 3458 (1993).

[29] D. T. Papageorgiou, On the breakup of viscous liquid threads, Phys. Fluids 7, 1529 (1995).

[30] R. F. Day, E. J. Hinch and J. R. Lister, Self-similar capillary pinchoff of an inviscid fluid, Phys. Rev. Lett. 80, 704 (1998).

[31] H. C. Lee, ‘‘Drop formation in a liquid jet,’’ IBM J. Res. Dev. 18, 364 (1974).

[32] R. M. S. M. Schulkes, Nonlinear dynamics of liquid columns: A comparative study, Phys. Fluids 5, 2121 (1993).

[33] R. M. S. M. Schulkes, Dynamics of liquid jets revisited, J. Fluid Mech. 250, 635 (1993).

[34] S. E. Bechtel, M. G. Forest, and K. J. Lin, Closure to all orders in 1D models for slender viscoelastic jets: An integrated theory for axisymmetric, torsionless flows, Stability Appl. Anal. Continuous Media 2, 59 (1992).

[35] J. Eggers and T. F. Dupont, Drop formation in a one-dimensional approximation of the Navier–Stokes equation, J. Fluid Mech. 262, 205 (1994).

[36] J. Eggers, Theory of drop formation, Phys. Fluids 7, 941 (1995).

[37] J. Eggers, Nonlinear dynamics and breakup of free-surface flows, Rev. Mod. Phys. 69, 865 (1997).

[38] E.D. Wilkes, S.C. Phillips and O.A. Basaran, Computational and experimental analysis of dynamics of drop formation, Phys. Fluids, Vol.11, No.12, 3577-3598, (1999).

[39] B.Ambravaneswaran, E.D. Wilkes, and O.A. Basaran, “Drop formation from a capillary tube: Comparison of one-dimensional and two-dimensional analyses and occurrence of satellite drops,” Phys. Fluids, Vol.14, No.8, 2606-2621, (2002).

[40] R. M. S. M. Schulkes, The evolution and bifurcation of a pendant drop, J. Fluid Mech. 278, 83 (1994).

[41] D. F. Zhang and H. A. Stone, Drop formation in viscous flows at a vertical

capillary tube, Phys. Fluids 9, 2234 (1997).

[42] O. A. Basaran, Nonlinear oscillations of viscous liquid drops, J. Fluid Mech. 241, 169 (1992).

[43] O. A. Basaran and D. W. DePaoli, Nonlinear oscillations of pendant drops, Phys. Fluids 6, 2923 (1994).

[44] E. D. Wilkes and O. A. Basaran, Forced oscillations of pendant (sessile) drops, Phys. Fluids 7, 1512 (1997).

[45] S. F. Kistler and L. E. Scriven, Coating flows, Applied Science, London,243. 1983

[46] J. M. Hyman, Numerical methods for tracking interfaces, Physica D 12, 396 (1984).

[47] C. Cuvelier and R. M. S. M. Schulkes, Some numerical methods for the computation of capillary free boundaries governed by the Navier–Stokes equations, SIAM ~Soc. Ind. Appl. Math. Rev. 32, 355 (1990).

[48]W. Tsai and D. K. P. Yue, Computation of nonlinear free-surface flows, Annu. Rev. Fluid Mech. 28, 249 (1996).

[49]G. Tryggvason and S.O. Unverdi, Computations of three-dimensional Rayleigh–Taylor instability, Phys. Fluids 2, 656 (1990).

[50] Hirt, C. W. and Nichols, B. D., Volume of fluid (VOF) method for the dynamics of free boundaries. J. Comput. Phys. 39, 201-225, (1981).

[51] J. R. Richards, A. N. Beris, and A. M. Lenhoff, Drop formation in liquid–liquid systems before and after jetting, Phys. Fluids 7, 2617 (1995).

[52] J. R. Richards, A. N. Beris, and A. M. Lenhoff, Steady laminar flow of liquid–liquid jets at high Reynolds numbers, Phys. Fluids 5, 1703 (1993).

[53] J. R. Richards, A. M. Lenhoff, and A. N. Beris, Dynamic breakup of liquid–liquid jets, Phys. Fluids 6, 2640 (1994).

[54] Fromm, J., Numerical calculation of the fluid dynamics of Drop-on-demand jets. IBM J. RES.DEVELOP, Vol. 28, No. 3, 322-333 (1984).

[55] Adams, R., and Roy, J., A one-dimensional numerical model of a drop-on-demand ink jet. Journal of Applied Mechanics, Vol. 53, 193-197, (1986).

[56] Bogy, D., and Talke, F., Experimental and theoretical study of wave propagation phenomena in drop-on-demand ink jet devices. IBM J. RES.DEVELOP, Vol. 28, No. 3, 314-321 (1984).

[57] Shield, T., Bogy, D., and Talke, F., A numerical comparison of one-dimensional fluid jet models applied to drop-on-demand printing. Journal of Computational physics, 67, 327-347 (1986).

[58] Wu, H., C., et al., Development of a three-dimensional simulation system for micro-inkjet and its experimental verification. Materials Science and Engineering A, 373, 268-278 (2004).

[59] Wu, H., C., et al., A numerical study of the effect of operating parameters on drop formation in a squeeze mode inkjet device. Modeling Simul. Mater. Sci. Eng., 13, 17-34 (2005).

[60] Shield, T., Bogy, D., and Talke, F., Drop formation by DOD ink-jet nozzles: A comparison of experiment and numerical simulation. IBM J. RES.DEVELOP, Vol. 31,

97-110 (1987).

[61] Chen, P., H., et al., Pressure response and droplet ejection of a piezoelectric inkjet printhead. International Journal of Mechanical Sciences, 41, 235-248 (1998).

[62] Bugdayci, N., Bogy, D., and Talke, F., Axisymmetric motion of radially polarized piezoelectric cylinders used in ink jet printing. IBM J. RES.DEVELOP, Vol. 27, No. 2, 171-180 (1983).

[63] Antohe, B., and Wallace, D., The determination of the speed of sound in liquids using acoustic resonance in piezoelectric tubes. Meas. Sci. Technol, 10, 994-998 (1999).

[64]Dijksman, J., F., Hydrodynamics of small tubular pumps. J. Fluid Mech., Vol. 139, 173-191 (1984).

[65]Shin, D., Y., Grassia, P., and Derby, B., Oscillatory limited compressible fluid flow induced by the radial motion of a thick-walled piezoelectric tube. J. Acoust. Soc. Am., 114(3), 1314-1321 (2003).

[66]Shin, D., Y., Grassia, P., and Derby, B., Numerical and experimental comparisons of mass transport rate in a piezoelectric drop-on-demand inkjet print head. International Journal of Mechanical Sciences, 46, 181-199 (2004).

[67]Shin, D., Y., Grassia, P., and Derby, B., Oscillatory incompressible fluid flow in a tapered tube with a free surface in an inkjet print head. Transactions of the ASME, Vol. 127, 98-109 (2005).

[68] W. J. Rider and D. B. Kothey, Reconstructing Volume Tracking, Journal of Computational Physics, 141, 112–152 (1998).

[69] J. U. Brackbill, D. B. Kothe, AND C. Zemach, A Continuum Method for Modeling Surface Tension, Journal of Computational Physics, 100, 335-354 (1992).

[70] C. W. Hirt AND B.D. Nichols, Volume of Fluid (VOF) Method for the Dynamics of Free Boundaries, Journal of Computational Physics, 39, 201-225 (1981).

[71] A. Theodorakakos AND G. Bergeles, Simulation of Sharp Gas-Liquid Interface Using VOF Method and Adaptive Grid Local Refinement Around the Interface, International Journal for Numerical Methods in Fluids, 45, 421-439 (2004).

[72] www.morgan-electroceramics.com

[73] FLUENT 6.2 User's Guide, FLUENT Inc.